

RICE UNIVERSITY

**Structural Analysis by Enhanced Raman Scattering**

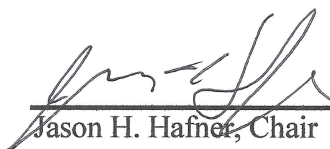
by

**James R. Matthews**

A THESIS SUBMITTED  
IN PARTIAL FULFILLMENT OF THE  
REQUIREMENTS FOR THE DEGREE

**Doctor of Philosophy**

APPROVED, THESIS COMMITTEE



---

Jason H. Hafner, Chair  
Associate Professor of Physics and  
Astronomy  
Associate Professor of Chemistry



---

Huey W. Huang  
Sam and Helen Worden Professor of  
Physics and Astronomy, Co-Chair for  
Graduate Admissions and Recruiting



---

Emilie Ringe  
Assistant Professor of Materials Science  
and Engineering  
Assistant Professor of Chemistry

HOUSTON, TEXAS  
January 2017

# ABSTRACT

## **Structural Analysis by Enhanced Raman Scattering**

by

**James R. Matthews**

Biological membrane structure is inherently complex, and understanding the structure of peptide chains inserted in membranes is vitally important for the development of effective diagnosis and treatments of diseases. Surface Enhanced Raman Spectroscopy (SERS) was used as a tool for studying lipid membrane structure in a natural fluid, room temperature environment.

Gold nanostructures focus light to a molecular length scale at their surface, creating the possibility to visualize molecular structure. Optical excitation of gold nanoparticles at their size and shape-dependent plasmon resonant frequency induces strong oscillations of the nanoparticle's free electron gas, leading to SERS – an enhancement of Raman scattering signals in a distance dependent manner at the molecular scale. This project utilizes gold nanorods, tuned to an excitation laser wavelength of 785 nm, as a substrate for lipid membranes so that their structure can be analyzed by SERS.

The surfactant cetyltrimethylammonium bromide (CTAB) that stabilizes nanorods was exchanged with the biologically relevant lipid dioleoylphosphatidylcholine (DOPC), and the insertion of the peptide residue tryptophan into the lipid membrane was observed using SERS for confirmation. Full

characterization of the lipid membranes was carried out, demonstrating a well ordered, gold supported bilayer.

SERS spectra also contain information on molecular position and orientation relative to the surface, but are difficult to interpret quantitatively. An analysis method that combines SERS and unenhanced Raman spectra with theoretical calculations of the optical field and molecular polarizability is introduced. Together these reveal the molecular orientation and position of surfactant layers on gold nanorods and of tryptophan in phospholipid bilayers. This method offers a new approach to analyzing lipid membrane molecular structure under ambient conditions, with microscopic quantities, and without molecular labels.

# Acknowledgments

“If I have seen farther than others, it is by standing on the shoulders of giants.” – Isaac Newton

I would like to thank my advisor, Jason Hafner for continuing to challenge me and encourage the pursuit of my PhD. His open honesty and friendly voice made for an exciting and fun research experience. Research can be a constant battle against failed experiments, but his mentoring made this battle a joy. My work felt impactful, exciting, meaningful, important, and challenging. For your patience with my endless tinkering between experiments, you are a saint. I gained so much from my PhD that is not included in this thesis because of the freedom I felt to explore and develop new skills on my own. That was as rewarding to me as the PhD itself, and as a result it has fostered interests that will carry me beyond grad school and through my career.

I have been so fortunate to have had labmates like Courtney Payne, and Steven Demmers. Despite my stubborn strive for independence, Courtney has been a constant source of knowledge and guidance starting from the moment I began my research, and continuing as I navigated my PhD, and pursued career opportunities. Sharing my research with a fellow physicist like Steven has been a sheer joy. His questions and ideas have added tremendous value to my research and cemented my understanding. I've had an overwhelmingly positive experience through my PhD, and I have no question that they contributed greatly to the wonderful time I've had.

I would not have even made it to Rice, let alone through a PhD, without the continuing love and support from my family. My girlfriend and partner Dipika Patel has been a foundation and inspiration to me. Your love, support, and encouragement have carried me through difficult setbacks to heights I never imagined. Your belief in me surpassed my own and I would not have come so far without you. I also would not be where I am without the unyielding love and support of my mother and step-father Melisse and Joe Kollmyer. I cannot begin to thank you for everything you have done and continue to do. Your belief in me gave me the confidence to pursue my dreams, while your support and sacrifice gave me the opportunity to do so. I would never have made it where I am today without you, and I am forever indebted to you for all you have done. Lastly, I'd like to thank my father and step-mother Don and Catherine Matthews and my two sisters Liz and Sarah. Your love and support has helped me through so many challenges along the way, and your encouragement helped me gain the confidence I needed to pursue this dream.

# Contents

<b>Acknowledgments</b> .....	<b>iv</b>
<b>Contents</b> .....	<b>vi</b>
<b>List of Figures</b> .....	<b>viii</b>
<b>List of Tables</b> .....	<b>xi</b>
<b>List of Equations</b> .....	<b>xii</b>
<b>Introduction</b> .....	<b>1</b>
1.1. Cell Membranes .....	1
1.1.1. Lipids .....	2
1.1.2. Peptides and Proteins.....	5
1.1.3. Vesicles and Supported Membranes.....	7
1.2. Membrane Structure Methods .....	8
1.2.1. Neutron and X-ray Scattering.....	9
1.2.2. Wide and Small Angle Scattering.....	10
1.2.3. NMR.....	11
1.2.4. Optical Absorption and Emission.....	12
<b>Raman Scattering and Surface Enhanced Raman Scattering</b> .....	<b>15</b>
2.1. Raman Scattering .....	15
2.2. Localized Surface Plasmon Resonance.....	18
2.3. LSPR Sensing.....	19
2.4. Surface Enhanced Raman Scattering .....	21
<b>Nanorod Supported Lipid Membranes</b> .....	<b>25</b>
3.1. Introduction.....	25
3.2. CTAB to DOPC Exchange.....	26
3.3. Experimental Methods.....	27
3.3.1. Preparation of Lipid Vesicles .....	27
3.3.2. CTAB Displacement on Gold Nanorods .....	28
3.3.3. SERS and LSPR Measurements .....	30
3.3.4. DLS Measurements.....	32

3.4. Results .....	32
3.4.1. Confirmation of CTAB Exchange .....	32
3.4.2. Nanorod Stability .....	35
3.4.3. Bilayer Structure and Phase Transitions .....	39
3.4.4. Bilayer Exchange .....	43
3.4.5. Bilayer Stability .....	45
<b>SABERS .....</b>	<b>51</b>
4.1. Analytical SERS .....	51
4.2. Predicting Structure .....	53
4.2.1. Raman and SERS Calculation .....	53
4.2.2. Electric Field Enhancement .....	57
4.2.3. Comparison with Experiment .....	58
<b>Tryptophan and DTAB Positions and Orientations in Gold Nanorod Supported Membranes.....</b>	<b>61</b>
5.1. Introduction.....	61
5.2. Methods and Materials .....	62
5.2.1. Materials.....	62
5.2.2. Sample Preparation .....	62
5.2.3. Raman Spectrometer.....	64
5.2.4. Electromagnetic Simulations .....	64
5.2.5. TDDFT Calculations .....	65
5.2.6. Ratio and Similarity Calculations .....	65
5.3. DTAB Orientation .....	67
5.4. DOPC Membrane Structure.....	70
5.5. Tryptophan Orientation and Position .....	72
<b>References .....</b>	<b>77</b>
<b>Appendix A: Source Code .....</b>	<b>83</b>

# List of Figures

<b>Figure 1: Molecular structures for lipids used in this project. A: DOPC B: DMPC with the same PC head group as DOPC but shorter saturated tail group. C: DOPG with the same DO tail group but different PG head group compared to DOPC. ....</b>	<b>4</b>
<b>Figure 2: The localized surface plasmon for a metal sphere (adapted with permission from Willets and Van Duyne).<sup>13</sup> Copyright 2007 Annual Reviews. ....</b>	<b>19</b>
<b>Figure 3: DLS measurement of DOPC SUVs in solution. ....</b>	<b>28</b>
<b>Figure 4: XPS results showing the presence of silver on gold nanorods. ....</b>	<b>29</b>
<b>Figure 5: Raman signal observed from empty lipid vesicles in solution. ....</b>	<b>31</b>
<b>Figure 6: The molecular structures of DOPC and CTAB are shown above. The SERS spectra of CTAB and DOPC coated gold nanorods with particular modes highlighted are also shown. Matching colors illustrate vibrational mode locations. ....</b>	<b>33</b>
<b>Figure 7: Area under the curve for the 760 cm<sup>-1</sup> headgroup peak of CTAB before (red) and after (blue) exchange with DOPC. ....</b>	<b>34</b>
<b>Figure 8: CTAB to DOPC exchange in three steps: gold nanorod SERS spectra showing the presence of (a) CTAB, (b) mixed CTAB and DOPC, and (c) DOPC. ....</b>	<b>35</b>
<b>Figure 9: Extinction spectra and matching photos of gold nanorod samples in CTAB, DOPC, and DOPC/DOPG mixture. ....</b>	<b>37</b>
<b>Figure 10: DLS analysis of gold nanorods supported in (a) 20mM CTAB, (b) 0.7 mM CTAB with ethonol, and (c) 2.5 mM DOPC/DOPG lipids. Insets represent the LSPR spectra for the same sample. ....</b>	<b>38</b>
<b>Figure 11: Illustration of the CTAB bilayer, and gel and fluid phase lipid bilayers. ....</b>	<b>41</b>
<b>Figure 12: LSPR peak wavelength vs temperature for DMPC/DOPG supported gold nanorods. ....</b>	<b>42</b>



- Figure 13: Three temperature scans of DMPC/DOPG showing the phase transition. Top scan is from Figure 12, and the bottom scan is from Figure 16d**  
 ..... 43
- Figure 14: Initial and final SERS spectra of DOPC/DOPG supported nanorods incubated with deuterated DOPC-d<sub>9</sub> vesicles at a 50 mol %.** ..... 44
- Figure 15: Full kinetic rate curves for the adsorption of DOPC-d<sub>9</sub> into the formed DOPC lipid layer on gold nanorods.** ..... 45
- Figure 16: Lipid layer structural transitions. a) SERS spectra of DOPC/DOPG supported gold nanorods at 10mg/mL and 0.001 mg/mL concentrations. b) LSPR peak wavelength of DOPC/DOPG lipids during dilution from 1.4 to 0.2 mg/mL concentration. c) SERS of DMPC/DOPG coated nanorods at 10 mg/mL and 0.006 mg/mL concentrations. d) LSPR peak wavelength of DMPC/DOPG coated nanorods. A bilayer transition is only shown in the higher concentration (bottom), and no transition for the lower concentration (top).**  
 ..... 47
- Figure 17: Dynamic light scattering of gold nanorods supported with DOPC/DOPG at a) 1, b) 0.1, and c) 0.01 mg/mL concentrations. Matching LSPR curves for each sample are shown as insets.**..... 49
- Figure 18: The gold nanorod nearfield optics of SABERS. A) A transmission electron micrograph of the gold nanorods used in the study that have 25nm diameter hemispherical endcaps. B) A scaled overlay of the calculated electric field lines (dashed) and the electric field magnitude (color scale) from an EM simulation, and the TDDFT optimized structure of DTAB on the tip of the nanorod (gray). The coordinate system for the orientation is also presented.**  
 ..... 53
- Figure 19: The electric field norm as a function of distance from the nanorod surface at A) 785 nm excitation wavelength, and B) an excitation wavelength corresponding to the 718 cm<sup>-1</sup> symmetric stretch of the DOPC headgroup.**...58
- Figure 20: TDDFT optimized structure of decyltrimethylammonium bromide (DTAB). Numerical labels indicate the positions and wavenumbers (cm<sup>-1</sup>) of the centers of vibration.**..... 67
- Figure 21: The DTAB surfactant structure according to SABERS. A) The SERS spectrum of DTAB on gold nanorods (red), the Raman spectrum of DTAB micells (blue) and the TDDFT spectrum for DTAB. The two peaks used for the**

calculation of  $R_{1-2}$  are labeled. B) The similarity  $S$  between theory and experiment for all accessible angles  $\theta$ ,  $\phi$ . The high band at  $\theta = 25^\circ$  and independent of  $\phi$  represents a tilted bilayer structure. .... 69

**Figure 22: SABERS analysis of the lipid membrane structure. A) The molecular structures analyzed in TDDFT were the phosphocholine headgroup positioned at  $5\text{\AA}$  above the gold particle surface, and the carbon double bond which was adjusted in  $z$ -position. B) The similarity map indicates a normally oriented fatty acid chain. C) The maximum similarity position at  $18\text{\AA}$ , which is  $13\text{\AA}$  past the headgroup..... 71**

**Figure 23: TDDFT optimized structure of tryptophan (TRP). Numerical labels indicate the positions and wavenumbers ( $\text{cm}^{-1}$ ) of the centers of vibration.... 72**

**Figure 24: The orientation and position of tryptophan in DOPC bilayers according to SABERS. A) SERS spectra of DOPC and tryptophan in DOPC (red). Unenhanced Raman of lyophilized tryptophan in DOPC (blue). TDDFT calculated Raman of tryptophan and DOPC. Numbered peaks were used in the analysis. B) The similarity map for all  $\theta$  and  $\phi$  at  $z = 13\text{\AA}$ . The peaks labeled a-d represent possible orientations. C) Similarity as a function of  $z$ -position. The blue curve represents the maximum similarity of all orientations. The red curve is the similarity at orientation a in part B. D) An illustration of the tryptophan position in the DOPC bilayer. The average positions of the lipid choline (red), phosphate (gold), glycerol (green), carbonyl (blue), alkane (gray), and  $\text{CH}_3$  (black) from SANS and SAXS measurements are included.<sup>85</sup> A coarse grain shaded figure of a relevant lipid structure is shown for reference.<sup>86</sup> ..... 73**

# List of Tables

<b>Table 1: Zeta potential of gold nanorods supported by CTAB and DOPC/DOPG.</b> .....	<b>36</b>
<b>Table 2: Ratio values at the optimal orientation for DTAB on gold nanorods.</b>	<b>70</b>
<b>Table 3: The ratio values for tryptophan at the optimal position and orientation in DOPC membranes.....</b>	<b>74</b>

# List of Equations

<b>Equation 2-1: The oscillating induced dipole of a molecule in an incident oscillating electric field.....</b>	<b>17</b>
<b>Equation 2-2: The general Mie extinction solution.....</b>	<b>20</b>
<b>Equation 2-3: General Mie solution for excitation of particles much smaller than the wavelength of light.....</b>	<b>20</b>
<b>Equation 2-4: The intensity of the enhanced Raman signal in SERS.....</b>	<b>23</b>
<b>Equation 4-1: Polarizability and anisotropy invariants definitions.....</b>	<b>54</b>
<b>Equation 4-2: The expression for the computed SERS count rate.....</b>	<b>55</b>
<b>Equation 4-3: Generalized form of the exponential electric field enhancement as a function of wavelength shift and z-position.....</b>	<b>57</b>
<b>Equation 4-4: The definition of Similarity used in comparing the theoretical and experimental peak ratios.....</b>	<b>60</b>

# Chapter 1

## Introduction

“Equipped with our five senses, we explore the universe around us and call the adventure Science.” – Edwin Hubble

### 1.1. Cell Membranes

Cell membranes define the boundary and maintain the interior and exterior environment differences. Biological membranes all have the same general structure: a thin lipid bilayer held together via noncovalent interactions. These lipid membranes also contain proteins which serve a variety of purposes. Some proteins act as sensors of external signals called receptors, which are common pharmaceutical drug targets for the treatment of disease. Other types of membrane proteins also exist which serve as structural links, or create membrane pores to assist in transmembrane transport. It is estimated that 30% of the proteins encoded in an animals genome are membrane proteins. Ion gradients also exist across

## 2

membranes which can be utilized by membrane proteins to synthesize adenosine triphosphate (ATP), a very important molecule for intercellular energy transfer.

These ion gradients help drive transmembrane transport, and in nerve and muscle cells these ion channels produce and transmit electronic impulse signals.

Membranes are not restricted to the boundary of the cell, they also encapsulate membrane enclosed organelles such as mitochondria and Golgi apparatus. For the majority of this project we will focus on forming and studying pure lipid membranes formed on gold nanorods, which will be described in greater detail later. In the final chapter, the amino acid Tryptophan will be introduced to the pure lipid membranes and its interaction with the membrane will be examined, but for now let's focus more on the lipid membrane specifically.

### **1.1.1. Lipids**

Cell membranes contain many molecules including membrane peptides, proteins, and cholesterol, but the primary building block of the cell membrane is the lipid. Lipids are a group of naturally occurring molecules which are amphiphilic and contain a polarized hydrophilic headgroup and a hydrophobic tail group. Due to their generic structure, when lipids are placed in water they naturally tend to orient themselves so that the hydrophobic tail groups are protected from the water, exposing only the hydrophilic head groups. This is accomplished either by the formation of either micelles, spherical aggregates of lipids where the lipids are arranged so that the head groups form the outer surface and the tail groups fill the inner volume, or by the formation of a bilayer vesicle membrane, where water is

### 3

contained within the vesicle and the membrane is made of a bilayer of lipid molecules with their head groups forming the inner and outer surfaces of the membrane and the tail groups of the inner and outer membrane leaflets facing toward each other. There are eight general classes of lipid molecules: fatty acids, glycerolipids, glycerophospholipids, sphingolipids, sterol lipids, prenol lipids, saccharolipids, and polyketides.

Fatty acids are made of a hydrophobic hydrocarbon chain, between 4 and 24 carbons in length, with a hydrophilic carboxylic acid headgroup. Glycerolipids are formed when usually two of the hydroxyl groups of a glycerol are esterified by a fatty acid.

Glycerophospholipids (or simply phospholipids) are the predominant component of the cell membrane. They are glycerolipids which have a phosphate group connected to the glycerol. For my research we use the following phospholipids: 18:1 (d9-Cis) Phosphatidylcholine (DOPC), 14:0 Phosphatidylcholine (DMPC), and 18:1 (d9-Cis) Phosphatidylglycerol (DOPG). In the abbreviations, the "D" indicates two acyl chains, the next letter indicates the length and degree of saturation of the acyl chains, and the last two letters indicate the headgroup. "PC" is phosphatidylcholine, a zwitterionic structure. "PG" is phosphoglycerol (negatively charged). Our "DO-" lipids are dioleoyl-, which means two 18 carbon chains with one double bond each. Carbon chains that contain a double bond are said to be unsaturated, since the double carbon bond limits the number of hydrogens that otherwise bond to the carbon chain. Carbon chains can bind together strongly in a

4

gel phase, or loosely in a fluid ( $L_{\alpha}$ ) phase based on the length of the chain, the number of hydrogens present in the chain, and the ambient temperature. For unsaturated carbon chains, fewer hydrogens means a lower binding energy between the chains so these chains tend to have lower phase transition temperatures. The DO- lipids used in this project have a fluid to gel phase transition below  $0^{\circ}\text{C}$ , ensuring that the lipids in our sample remain in the fluid phase for all experiments. For experiments where the phase transition was studied, DM- lipids were substituted which contain two saturated tail groups and has a phase transition temperature near room temperature.

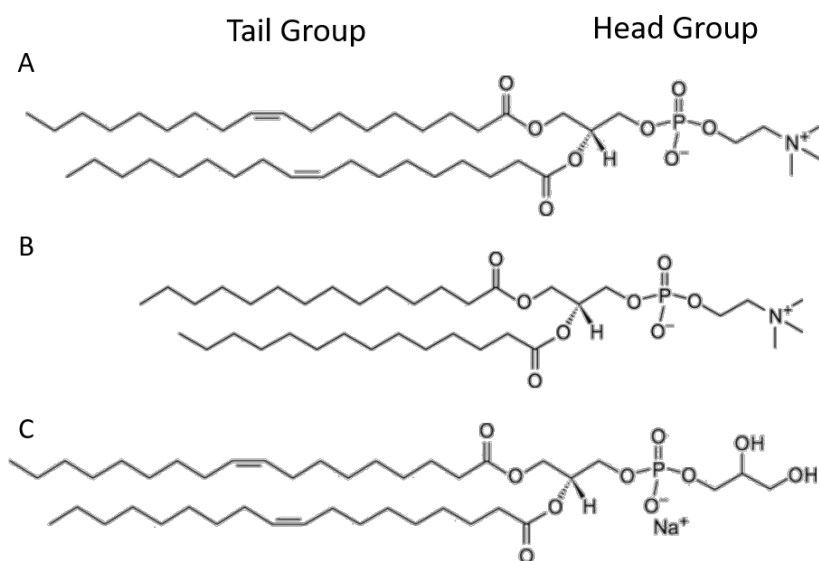


**Figure 1: Molecular structures for lipids used in this project. A: DOPC B: DMPC with the same PC head group as DOPC but shorter saturated tail group. C: DOPG with the same DO tail group but different PG head group compared to DOPC.**

Phospholipids are the main components of cell membranes and remain the focus of the work presented here. Other lipid types have more specialized purposes.



## 5

Sphingolipids are a diverse group of lipids which contain a fatty acid chain and a sphingoid base backbone. Because they tend to have long and saturated fatty hydrocarbon chains, sphingolipids are commonly found in lipid rafts, regions of gel phase lipids in an otherwise fluid membrane, along with cholesterol. The thicker lipid rafts can better accommodate some membrane proteins, but are not studied in this work. Cholesterol is an example of a membrane lipid known as a sterol lipids. They are a class of steroid with hydroxyl group on the A-ring, and serve as signaling molecules and hormones. Saccharolipids are made from fatty acid chains connected to a sugar backbone. Prenol lipids contain prenyl (3-methyl-2-buten-1-ol). Polyketides which are a class of secondary metabolites which have diverse structures. Variations of polyketides are used as anti-microbial, anti-cancer, and anti-parasitic agents.

### **1.1.2. Peptides and Proteins**

Peptides are molecules which are made of at least two amino acids bound together by a peptide bond. The peptide bond is formed between the ammonia group of one amino acid and the carboxyl group of another by the creation of a water molecule. A protein is a polymer of amino acids where the peptide bonds create the ...N-C-C-N-C-C-N... protein backbone. In the protein backbone sequence, the alpha carbon contains the R group and a hydrogen, where the R group represents any of the 20 naturally occurring amino acids. These amino acids bind to the protein backbone in specific sequences which dictate the folding and ultimately the structure of the protein or peptide.

## 6

Many proteins and peptide chains fold into a helical structure, the alpha helix, which is a common structural motif for proteins, with beta sheets being another. In terms of thermodynamics, the protein will always assume a structure such that the free energy  $G$  is minimized. The alpha helix structure is enthalpically driven by the formation of hydrogen bonds between amine and carboxyl groups along the backbone chain. The entropy is dominated by the conformational freedom of the amino acid side chains. The alpha helix conformation restricts the freedom of the different side chains, reducing their entropy compared to a random coil. This entropic effect on the free energy is smaller than that of the hydrogen bond formation. Different side chains present different configurational entropies which helps determine what sequences tend to form an alpha helix.

Membrane proteins interact as either integral or peripheral proteins. Integral membrane proteins include transmembrane proteins and integral monotopic proteins. Peripheral membrane proteins interact temporarily with the membrane either through amphipathic alpha-helix parallel to the membrane plane, through interaction of a hydrophobic loop, through a covalent bond with a membrane lipid known as lipidation, or through electrostatic or ionic interaction with the membrane. Integral monotopic proteins bind similarly yet permanently with one side of the membrane. Transmembrane proteins are integral membrane proteins that permanently attach to and span the membrane. These proteins are often responsible for pore formation and the regulation of transportation across the membrane.

### 1.1.3. Vesicles and Supported Membranes

Following the importance of cell membranes in mediating environmental interactions for cells, various methods exist for studying membrane models. The fluid mosaic model of lipid membranes set forth by S. J. Singer and G. L. Nicolson treats the cell membrane as a two dimensional liquid with restricted lateral diffusion.<sup>1</sup> Earlier, cell membranes were described as naturally forming vesicles in solution, and much has been learned about membranes by studying single or multiple component lipid vesicles in solution. Another common method for studying membranes is to study a supported lipid bilayer which has been absorbed onto flat surfaces. Supported lipid bilayers (SLBs) are formed a variety of ways and on a variety of substrates the most common of which are glass and mica, while SLB formations on gold are more difficult but can be made easier with the use of thiols.<sup>2</sup> Reportedly the most important factor in determination of SLB formation on substrates is the surface chemistry between the lipids and the substrate surface.<sup>2</sup> The theory set forth by Seifert and Lipowsky describes the surface binding to be a balance between the adhesion energy and the vesicle's curvature energy.<sup>3,4</sup> For silica based substrates such as glass, SLBs have been shown to exhibit two dimensional diffusion across the substrate surface through fluorescence recovery after photobleaching (FRAP).<sup>5</sup> This project will revisit supported lipid layers on gold nanorods in Chapter 3. In that chapter, experimental evidence will be shown that DOPC binds ionically to the bromide-gold interface similar to CTAB to form supported membranes, that these lipid layers diffuse easily with vesicles in solution, and that an affinity between the gold surface and the lipid molecule exists so that a

critical concentration of lipid vesicles is required to be present in solution to maintain stable lipid layers on gold nanorods.

## 1.2. Membrane Structure Methods

Experimental study of the cell membrane structure has been of interest for some time, and provides an extreme challenge due to the small scale, varied structure, and dynamic character of lipid membranes. This means that fluctuations within the membrane must be taken into consideration when analyzing experimental results.<sup>6</sup> Additionally, studying such membranes *in situ* or in naturally existing conditions (such as in solution at room temperature) establishes strict experimental constraints. That is not to say that valuable information cannot be obtained from experiments that do not maintain these conditions, only that these conditions represent the ideal scenario. Experimental methods that can be useful include both optical and transmission electron microscopies which can be useful for directly observing structures and phases, of which optical microscopy is the most accommodating for *in situ* experiments. Other methods include optical rotary dispersion and circular dichroism, both of which are absorption spectroscopic techniques which examine the interaction of polarized light with optically active molecule. Many other methods exist for studying membrane structures, and below are four sections which broadly outline some of the more popular methods used, with an emphasis on methods used for studying the lipid membrane structure.

### 1.2.1. Neutron and X-ray Scattering

Scattering is a broad term used to describe the constructive interference of waves scattered or reflected by atoms in the sample. The physics of scattering is similar for both electromagnetic waves in X-ray scattering or the quantum wave properties of a particle in the case of Neutron scattering. The key to interpreting scattered light from assemblies of sub-micron molecules is repetition. The simplest case of repetition is a pure crystal lattice which exactly and infinitely repeats. It is this repetition that allows for a seamless transformation from real to reciprocal space.

Diffraction is a similar phenomenon where the reflection of a wave from repeating structures creates constructive interference dictated by Bragg's law:

$$\lambda = 2d \sin(\theta)$$

where  $\theta$  represents the angle of the incident wave of wavelength  $\lambda$ . Constructive interference is created when the spacing between the planes of atoms  $d$  satisfies the equation above. Neutron diffraction is especially useful for membrane structure since specific regions of lipid molecules can be deuterated in preparation to act as a contrast agent while leaving the sample nearly unchanged physically and chemically.<sup>6</sup>

For the study of protein structure, the proteins are crystalized and studied with X-ray or neutron scattering. The lipid bilayer itself cannot be crystalized, but it can form ordered multilamellar layers (MLVs) that are amenable to analysis by

X-ray and neutron scattering.<sup>6</sup> Especially for fully hydrated membranes in the fluid  $L_\alpha$  phase, no crystalline state physically exists, which limits the scattering and diffraction methods to multilamellar layers. For this reason, the majority of lipid structures used in X-ray and neutron experiments utilize multilamellar lipid layers, and although not preferred to unilamellar vesicles, they still provide valuable information for studying the lipid layer thickness at fluid and gel phases.<sup>6</sup> The interbilayer interactions in these MLVs must be considered since such interactions could alter the structure of the membrane, although these interactions are small enough not to affect the structure of a fully hydrated layer.<sup>6</sup>

### 1.2.2. Wide and Small Angle Scattering

Small angle X-ray scattering (SAXS) and small angle neutron scattering (SANS) both rely on the same fundamental principles as X-ray and neutron scattering and diffraction discussed above, except with smaller angles of scattering usually only  $0.1-10^\circ$  from the incident collimated beam. The scattered intensity is represented as a function of the magnitude of the scattering vector  $q = 4\pi \sin(\theta) / \lambda$ . Small angle scattering deals with wavenumbers smaller than usual for typical Bragg diffraction so that the scattered intensity follows Porod's law:

$$I(q) \approx Sq^{-4}$$

The surface area  $S$  of the scattering particles is therefore determined accordingly. In small angle scattering, the incident X-rays or neutrons are shone through a sample of randomly oriented particles rather than in a pure crystal. These particles can be

suspended in solution such as metallic nanoparticles or lipid vesicles.<sup>7</sup> Unilamellar vesicles have been studied more recently with neutron scattering,<sup>8-10</sup> however low signal to noise ratios limit the resolution of these measurements so that they provide little benefit over the MLV studies.<sup>8</sup>

### 1.2.3. NMR

Nuclear magnetic resonance (NMR) is a spectroscopic technique that provides location information for hydrogen, carbon, nitrogen, and phosphorus atoms in the sample. The basic theory behind NMR relies on the atomic magnetic field generated by the proton's spin. By exposing the proton's magnetic moment  $\mu$  to an external field  $H_0$ , the magnetic moment will align at an angle  $\theta$  either with or against the external field so that the potential energy of the state is either  $-\mu H_0 \sin\theta$  or  $\mu H_0 \sin\theta$ , and the difference in the energy levels is  $2\mu H_0 \sin\theta$ . This energy difference corresponds to a radiation frequency of  $\nu = 2\mu H_0 \sin\theta/h$  where  $h$  is Planck's constant. By absorbing energy of this frequency, the magnetic moment is said to 'flip' from one orientation to the other. For atoms containing more than one proton, the magnetic spin number  $I$  determines the number of different orientations, *ie* energy levels, an atom can assume as being  $2I + 1$  where  $I$  is always an integer multiple of  $\frac{1}{2}$ . Additionally, the orbiting electrons also feel an inclination to rotate in the presence of  $H_0$  which induces another magnetic field. The field from the electrons screens the external field from the nucleus so that the screened field the nucleus sees is  $H_{eff} = (1 - \alpha)H_0$  where  $\alpha$  is called the screening constant. Also, the presence of nearby atoms affects the field seen by the nucleus, and it is this

interaction with the environment that provides valuable information from NMR.

The shift in resonance frequency due to these environmental interactions is called the chemical shift. The chemical shift is measured as a shift from the resonance line of some standard reference material which is added to the sample. Many types of environmental interactions can affect the chemical shift in a molecule. The electronic structure of the molecule itself, that is the local electron arrangement and its resulting screening effect can change the chemical shift. Similarly, the presence of a free electron such as an ionic charge can cause a similar shift in the chemical shift. If two molecules interact, the electron distribution of one can screen the other molecule. In chemically dynamic situations it is clear that the chemical shift will change as a function of time so chemical interactions within a sample can also affect the chemical shift. Carefully studying the chemical shifts in a sample can provide conformational information based on the revealed molecular interactions.

For probing membrane structure, introduction of deuterated water into the sample and measuring regions with no deuterated water tells you the membrane thickness. Since the chemical shift is sensitive not only to atomic sequence but also conformation in a molecule, NMR has great potential for studying peptide and protein structures. By studying the chemical shifts of a protein in a membrane, information can be deduced about the protein's position and folded structure.

#### **1.2.4. Optical Absorption and Emission**

Light is composed of oscillating, mutually perpendicular electric and magnetic waves. When light interacts with a molecule, the light can either be either



## 13

scattered elastically, scattered inelastically, or absorbed. The case of scattering will be addressed in the next chapter. In the case of absorbed light, the molecule is excited to a higher energy level, then either transmits that energy to nearby molecules as heat, or the molecule may reemit the light as fluorescence. Molecules contain discrete energy levels representing the electronic energy levels of the molecule's electron distribution. The absorption of energy is most probable when the amount of absorbed energy represents the difference between two discrete energy levels in the molecule. An electronic energy transition represents the moving of an electron to a different orbital state through the transaction of energy. The probability of absorption at a single wavelength is described by the molar absorption coefficient  $\epsilon$ . If incident light of intensity  $I_0$  is shone on the sample of molecules of thickness  $d$  and molar concentration  $c$ , the intensity of transmitted light follows the Beer-Lambert law

$$I = I_0 10^{-\epsilon dc}$$

Since the absorption energies and associated probabilities rely on the structure and environment of the molecule, absorption spectroscopy is a very useful tool for studying molecular structures. In some molecules the absorption of light is followed by the emission of light at a lower frequency. This emission is known as fluorescence. When a molecule absorbs light and is excited to a higher energy state, the molecule will dissipate that gained energy either as heat or through radiative transition in the case of fluorescence. The ability for a molecule to fluoresce depends on the atomic arrangement of the molecule and the resulting energy levels

within the molecule. Fluorescing molecules (fluors) are rare since discipation of absorbed energy is most likely as heat. However the use of fluors as markers to study membrane structure has been very successful. In protein studies, the fluorescence of tryptophan, tyrosine, and phenylalanine depends strongly on their environment and are therefore useful for conformational studies. Other extrinsic fluors have been discovered that can be added to the target molecule, however careful precautions must be taken to ensure that the fluor is tightly bound to a specific location on the target molecule, and must not affect the features of the molecular conformation, while remaining sensitive to the environment. For membrane structures, fluors have also been useful in demonstrating lipid fluidity and diffusion through use of fluorescence quenching where the fluor is overexposed to incident light to the point that the fluor becomes radiation-less.

Another interesting application of molecular absorption of light is the study of the wavelength dependence of absorbed polarized light by a molecule such as in optical rotary dispersion (ORD) and circular dichroism (CD). Similarly, the difference of absorption of linearly polarized light oriented parallel and perpendicular to a given axis is the basis for linear dichroism spectroscopy (LD). For studying tryptophan in lipid membranes, LD spectroscopy has been used to determine the tryptophan orientation by aligning stacks of lipid membranes by sheer flow.<sup>11</sup>

# Raman Scattering and Surface Enhanced Raman Scattering

“If you want to find the secrets of the universe, think in terms of energy, frequency, and vibration.” – Nikola Tesla

### 2.1. Raman Scattering

Raman scattering was discovered in the late 1920's and is a vibrational spectroscopy technique where incident light is scattered off a molecule of interest.<sup>12</sup> First let's imagine the molecule as a collection of atoms, and count the number of vibrational modes in the molecule. For a given molecule containing  $N > 1$  atoms, there exists  $3N$  degrees of freedom in the molecule. Each degree of freedom can be categorized into either translation, rotation, or vibration. For the  $3N$  degrees of freedom, there are three translations which correspond to translating the molecule along either the x, y, or z directions. For non-linear molecules, three of the

## 16

rotational degrees of freedom correspond to rotation of the entire molecule about the x, y, or z-axis. Therefore, the number of vibrational modes in a non-linear molecule with  $N > 2$  atoms is  $3N - 6$ . For a linear molecule, there exists a rotationally symmetric axis so that only 2 degrees of rotational freedom exist, and the total number of vibrations for a linear molecule is  $3N - 5$ . The typical frequency of molecular vibrational modes ranges between  $10^{12}$  to  $10^{14}$  Hz corresponding the energies in the infrared region of the electromagnetic spectrum. Molecules in the sample can be excited to higher energy states by the absorption of specific amounts of energy. The use of infrared incident light ensures that the energy exchanged will probe vibrational energy transitions within the molecule, since electronic energy state transitions required higher energy. IR spectroscopy therefore identifies molecules through their specific vibrations.

When visible light interacts with a molecule it may be absorbed due to electronic transitions. If no electronic transition of the appropriate energy exists, the light will be predominately scattered at the same energy (Rayleigh scattering). A small fraction of scattered visible light may lose or gain some energy from a vibrational mode in the molecule so that the scattered light may be shifted to either a lower energy in the case of Stokes, or to a higher energy in the case of Anti-Stokes. Anti-Stokes Raman scattering is a very useful tool for carefully studying the temperature of a sample. The majority of the work done here was in studying the Stokes Raman scattering situation.

To delve further into the mechanism of Raman scattering, consider the classical treatment of a molecule as a collection of charges. If a molecule is placed in an external electric field, an induced dipole in the molecule is created and described by  $\mu_{ind} = \alpha E$ . In the case of incident light, the external electric field oscillates so that  $E = E_0 \cos 2\pi\nu t$  where  $\nu$  is the frequency of vibration and  $t$  is time. Therefore, the induced dipole from this oscillating field is

$$\mu_{ind} = \alpha E_0 \cos 2\pi\nu t$$

The polarizability of the molecule is a function of the atomic arrangement in the molecule and therefore changes as the molecule vibrates. Therefore,  $\alpha$  will vary at the vibrational frequency of the atomic bond so that

$$\alpha = \alpha_0 + (\Delta\alpha) \cos 2\pi\nu_0 t$$

where  $\alpha_0$  is the polarizability at equilibrium,  $\Delta\alpha$  is the maximum polarizability deviation, and  $\nu_0$  is the natural vibration frequency. Combining these results, we see that

$$\mu_{ind} = \alpha_0 E_0 \cos 2\pi\nu t + \frac{1}{2} \Delta\alpha E_0 [\cos 2\pi(\nu + \nu_0)t + \cos 2\pi(\nu - \nu_0)t]$$

***Equation 2-1: The oscillating induced dipole of a molecule in an incident oscillating electric field.***

In this expression, the induced dipole oscillation at frequency  $\nu$  represents Rayleigh scattering, and the oscillation frequencies  $\nu + \nu_0$  and  $\nu - \nu_0$  represent the

Stokes and Anti-Stokes Raman frequencies respectively. In a closely related phenomenon, IR spectroscopy focuses on the absorbed infrared light by a vibrating molecule by studying the transmitted IR light through a sample. Raman scattering focuses on the scattering of this light by a vibrating molecule. Vibrational transitions in which the dipole moment of the molecule changes are said to be IR active and lead to the absorption of IR light. Vibrational transitions where the polarizability of the molecule changes are Raman active and lead to scattering of energy shifted light as described above.

## **2.2. Localized Surface Plasmon Resonance**

The oscillating electric field of incident light can induce a standing wave in the free electron gas of a metal if the frequency of light is correct for the size, shape and conductivity of the metal. This process describes the effects observed in antennas used every day in radio application. As the size of the antenna is reduced, the electrical resonant frequency of that antenna is increased.

In the case of a metallic particle smaller than the wavelength of light, the confined conduction electron oscillation is spatial. For nanoscale metallic particles, the dielectric function of the material plays an important role in the formation of a localized surface plasmon resonance (LSPR). Particles composed of materials such as noble metals which have a small positive imaginary, and negative real dielectric constant are capable of supporting such a surface plasmon. The size, shape, composition, and environment of these materials determines the exact plasmon

resonant frequency, for example silver nanoparticles can have plasmon resonant frequencies reaching into the UV, while gold nanoparticles of the same shape and size can have a lower resonant frequency within the visible spectrum of light. The study of these surface bound, free electron oscillations in nanostructures is called plasmonics.

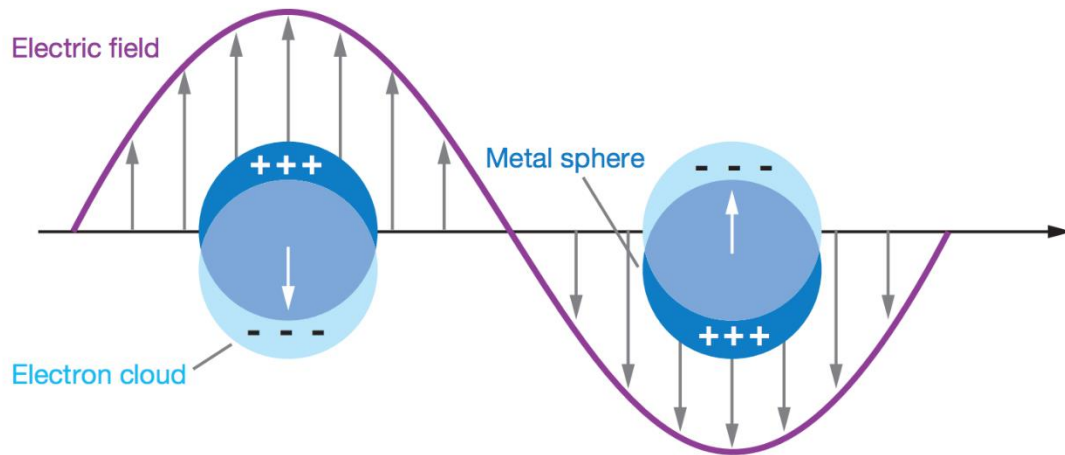


*Figure 2: The localized surface plasmon for a metal sphere (adapted with permission from Willets and Van Duyne).<sup>13</sup> Copyright 2007 Annual Reviews.*

### 2.3. LSPR Sensing

According to Mie theory, the extinction (defined as the sum of absorption and scattering) of a spherical particle is given by

$$\sigma_{ext} = \frac{\lambda^2}{2\pi} \sum_{L=1}^{\infty} (2L + 1) \text{Re}(a_L + b_L)$$

$$a_L = \frac{\mu m^2 j_L(mx) [x j_L(x)]' - \mu_1 j_L(x) [mx j_L(mx)]'}{\mu m^2 j_L(mx) [x h_L^1(x)]' - \mu_1 h_L^1(x) [mx j_L(mx)]'}$$

$$b_L = \frac{\mu_1 j_L(mx) [x j_L(x)]' - \mu j_L(x) [mx j_L(mx)]'}{\mu_1 j_L(mx) [x h_L^1(x)]' - \mu h_L^1(x) [mx j_L(mx)]'}$$

***Equation 2-2: The general Mie extinction solution.***

Here,  $m$  is the relative index of refraction of the material,  $j$  and  $h$  are the spherical Bessel and Hankel functions, and  $\mu$  is the magnetic permeability. For spherical particles, much smaller than the wavelength of light, the general Mie solution for the extinction can be simplified to:

$$\sigma_{ext}(\omega) = \frac{9\omega}{c} \epsilon_m^{3/2} V \frac{\epsilon_2(\omega)}{[\epsilon_1(\omega) + 2\epsilon_m]^2 + \epsilon_2(\omega)^2}$$

***Equation 2-3: General Mie solution for excitation of particles much smaller than the wavelength of light.***

where  $\epsilon_m$  is the dielectric constant of the surrounding medium, and  $\epsilon_1(\omega)$  and  $\epsilon_2(\omega)$  are the real and imaginary components of the dielectric function of the particle's material. Certain noble metals such as gold, silver, and copper have negative real components in their dielectric function which gives their extinction vs wavelength curve a Lorentzian peak centered at the plasmon resonance frequency, or where the negative real part of the metal's dielectric constant equals twice that of the medium. The exact wavelength of the peak position of the localized surface plasmon resonance is therefore also dependent on the surrounding medium index



of refraction as shown in Equation 2-3, which has been used as an optical transducer in applications. As an example, by carefully monitoring the LSPR peak wavelength, the binding of analytes to receptors can be monitored.<sup>14-16</sup>

Additionally, phase transitions within lipid layers on the surface of a nanoparticle can also effect the surrounding index. It is known that the dielectric function (or refractive index) of a lipid membrane in solution changes during the gel to fluid phase transition due to the reordering of the molecules during the transition, which affects the molecular polarizability at optical frequencies.<sup>17</sup> It is also known that melting paraffin wax decreases the index of refraction in the near IR due to the reordering of the carbon chain tail groups. However, lipid membranes have the added complexity that they are optically birefringent. Birefringence  $\Delta n$  is defined as the extraordinary index of refraction  $n_e$  which is parallel to the optical axis, minus the ordinary index of refraction  $n_o$  which is perpendicular to the optical axis, or

$$\Delta n = n_e - n_o$$

Studies have shown that the birefringence of DMPC lipid bilayers decreases during the gel to fluid phase transition.<sup>17</sup>

## 2.4. Surface Enhanced Raman Scattering

The formation of a localized surface plasmon in metallic nanostructures concentrates light to a nanometer scale near the nanoparticle surface due to the resonant oscillations of the free electrons.<sup>18</sup> These plasmon resonances greatly

increase the optical field intensity at the nanoparticle surface often referred to as surface enhancement, and leading to their application in surface-enhanced spectroscopy.<sup>19</sup> By positioning a molecule at the surface of a nanostructure, the intense surface enhanced field can be utilized. This concentrated electromagnetic field amplifies the Raman scattered light for nearby molecules in a technique known as surface enhanced Raman scattering (SERS).<sup>20</sup>

To understand the physics more completely, we will start by considering a molecule on the surface of a spherical particle. If our molecule is treated as a classical dipole, then illumination with a plane wave of frequency  $\omega_0$  will cause the dipole to radiate at the Raman frequency  $\omega$ . We can then write the dipole moment of our radiating molecule as  $\mathbf{p}(\mathbf{r}', \omega) = \boldsymbol{\alpha} \cdot \mathbf{E}_p(\mathbf{r}', \omega_0)$  where  $\boldsymbol{\alpha}$  is the polarizability tensor for the molecule.<sup>19, 21</sup> To calculate the magnitude of the scattered field enhancement due to the presence of the metal sphere, let's start by calling the enhancement factor  $g$ . The magnitude of the field radiated by the particle is

$$E_{LM} = gE_i$$

where  $E_i$  is the magnitude of the incident field and  $E_{LM}$  is the Lorentz-Mie calculated scattered field. This is the average scattered field from the particle so that on average, a molecule on the surface will scatter a Raman field of magnitude

$$E_{sc} \propto \alpha E_{LM} \propto \alpha g E_i. \quad 22$$

To clarify,  $E_{LM}$  is the field scattered by the particle, while  $E_{sc}$  is the field scattered by the molecule on the particle's surface. Similar to the way the incident

field is enhanced by the particle, the frequency shifted Raman scattered light from the molecule is also enhanced by the particle by an enhancement factor  $g'$ . We use the  $g'$  here to emphasize that since the Raman scattered light is at a shifted frequency  $\omega$ , the enhancement factor will differ from  $g$ . The magnitude of the SERS scattered field is then given as  $E_{SERS} \propto g'E_{sc} \propto \alpha g g' E_i$ .<sup>22</sup> The enhancement factors  $g$  and  $g'$  are calculated through the appropriate boundary value calculation. The SERS intensity is then given by the square of the field magnitude so that we get

$$I_{SERS} \propto |\alpha'|^2 |g g'|^2 I_0.$$
<sup>22</sup>

***Equation 2-4: The intensity of the enhanced Raman signal in SERS.***

In this description, the metallic particle behaves like an antenna by both focusing the light onto the surface and simultaneously broadcasting the Raman scattered light. In other situations involving nanostructures positioned closely together, the coupled near fields generate 'hot spots' where the gain of the broadcasted signal is sufficient enough that vibrational spectra from a single molecule can be recorded.<sup>23</sup>

SERS has been widely pursued for various applications of biological and chemical sensing. Such pursuits have largely focused on development of metallic substrates that provide large enhancements and high detection sensitivity.<sup>23-28</sup> The localized surface field enhancement is polarized relative to the surface of the nanostructure and also contains a strong distance dependence which could provide structural information on the surrounding layer. As an example, the surfactant

structure on gold electrodes has been studied with SERS, and a structural transition was detected by SERS in the surfactant layer on gold nanorods.<sup>29, 30</sup>

One benefit to biological studies is that SERS provides molecular specificity without the need for labels or dyes, and could therefore be a powerful tool for the study of biomembranes structure. Additionally, SERS spectra are capable of being collected from particles suspended in solution at ambient temperature, which is advantageous in the study of biological structures where many current methods are restricted to less natural environments.

# Nanorod Supported Lipid Membranes

### 3.1. Introduction

The utilization of phospholipid bilayers on nanoparticles as model biomembranes has been widely pursued. In terms of biological applications, lipid coatings can help stabilize nanoparticles in aqueous solution, as well as help facilitate targeting and circulation *in vivo*. Additionally, functionalized nanoparticles can be used in applications such as biomedical assays. The nanoparticles themselves can be of various materials such as gold, silver, silica, iron oxide, semiconductors, or polymer depending on the application, and material choice is usually dominated by strategies associated with different surface chemistries.<sup>31-33</sup>

Lipid presence at the surface of nanoparticles can be confirmed using several methods including surface charge from zeta-potential measurements, size changes by dynamic light scattering (DLS), composition analysis by X-ray photoelectron

spectroscopy (XPS), and direct visualization by transmission electron microscopy (TEM). While these and other methods can confirm the presence of lipids at the surface, they cannot demonstrate a well ordered lipid bilayer. There are ways in which bilayer structures can be indirectly verified such as by biochemical assays and molecular probes.<sup>34, 35</sup> While TEM might show a layer of the appropriate thickness, it cannot prove the lipid formed a well ordered bilayer in solution.<sup>36</sup> Differential scanning calorimetry (DSC) provides some of the most convincing evidence of a natural bilayer structure by detecting the fluid/ gel phase transition of the acyl chain region.<sup>37</sup> Additionally, DSC of lipid coated silica particles has shown that the phase transition temperature of the lipids is similar to that of empty vesicles.<sup>38</sup> Since such small amounts of lipids are involved in nanoparticle samples, DSC is difficult to apply for these samples.

### **3.2. CTAB to DOPC Exchange**

Numerous methods of coating gold nanoparticles with lipids have been demonstrated in the past.<sup>34-36, 39-49</sup> These methods include first coating the nanoparticle with alkanethiol self-assembled monolayers as the inner layer, then exposing the hydrophobic particles to lipids in solution to assemble the outer layer.<sup>34, 41, 42</sup> Such hybrid bilayers exhibit natural biological interactions involving the outer layer such as drug molecule interaction, and lipid exchange with vesicles in solution.<sup>34, 42</sup> A similar strategy is to use a thiol-modified lipid for the lower layer. This method has been shown to create lipid membranes that are capable of capturing lipoproteins from solution.<sup>35, 40</sup> For each of these methods, the lower leaf

of the lipid bilayer is firmly bound to the gold surface which could restrict studies where a fully fluid, natural bilayer is required. Another approach is to rely upon the attraction of halide ions to the gold nanoparticle surface. In the case of cetyltrimethylammonium bromide (CTAB), bromide ions are bound to the gold surface and the trimethylammonium headgroup is electrostatically attracted to the nanorod surface. Similarly, the headgroup of the common lipid phosphatidylcholine terminates with a very similar quaternary ammonium cation, so that these lipids should also be electrostatically attracted to the bromide ion on the nanoparticle's surface. Several groups have exchanged CTAB for lipids by simply suspending the nanorods in concentrated lipid vesicle solutions.<sup>39, 43, 44, 46</sup>

### **3.3. Experimental Methods**

#### **3.3.1. Preparation of Lipid Vesicles**

The phospholipids 1,2-dioleoyl-sn-glycero-3-phospholipid (DOPC), 1,2-dioleoyl-sn-glycero-3-phospho-(1'-rac-glycerol) (DOPG), 1,2-dimyristoyl-sn-glycero-3-phosphocholine (DMPC), and 1,2-distearoyl-sn-glycero-3-phosphocholine-N,N,N-trimethyl-d<sub>9</sub> (DOPC-d<sub>9</sub>) were purchased in chloroform from Avanti Polar Lipids. These lipids were then prepared by drying the chloroform solution under a stream of inert argon gas, then hydrating the dried lipid in DI water to bring the lipid concentration to 10 mg/mL. These hydrated lipids were then gently bath sonicated until the formation of small unilamellar vesicles (SUVs) was observed. The size of the SUVs was checked using dynamic light scattering (DLS)

with a Malvern zen 3600 Zetasizer. The resulting diameter of the measured SUVs was centered around 30 nm, which is a typical and expected size for vesicles prepared by sonication (Figure 3).

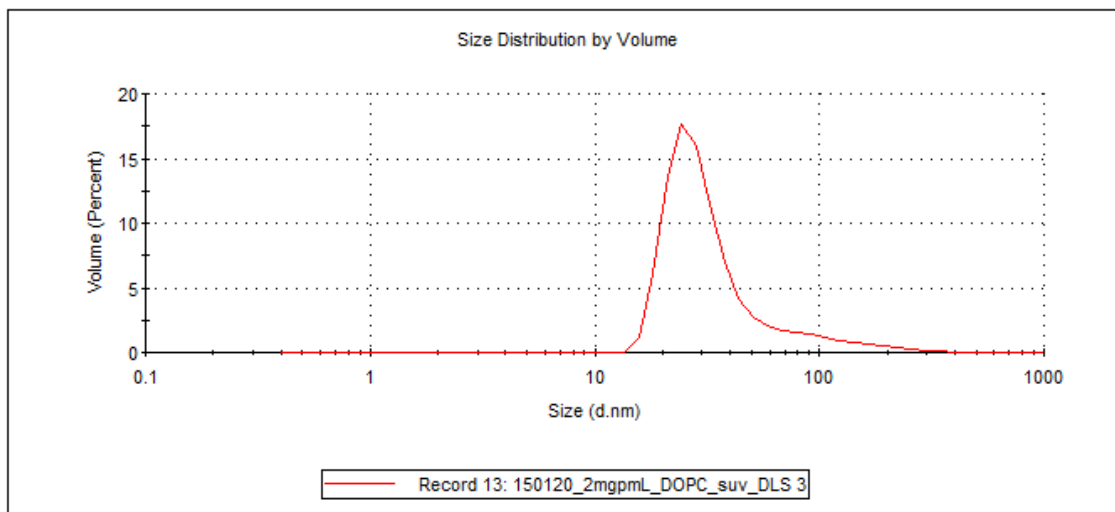


*Figure 3: DLS measurement of DOPC SUVs in solution.*

### 3.3.2. CTAB Displacement on Gold Nanorods

CTAB stabilized gold nanorods (50 nm diameter, 200 nm length, 800 nm peak absorbance, part no. A1250-800) were purchased from Nanopartz. These rather large nanorods were chosen due to their relatively large radius of curvature which is more amenable for a lipid bilayer surface. The nanoparticle concentration of 17.2 pM gave a peak plasmon absorbance of 1. This absorbance was used later as a metric for concentrating the nanorods. The nanorods were dried onto a glass substrate and studied under X-ray photoelectron spectroscopy to check for the presence of silver, which is used in the process of high yield nanorod synthesis.<sup>50, 51</sup>



The presence of silver was detected via a peak at the Ag 3d binding energy. The ratio of the silver to gold Au 4f peak (Figure 4) is similar to previous studies on high yield gold nanorods.<sup>52</sup>

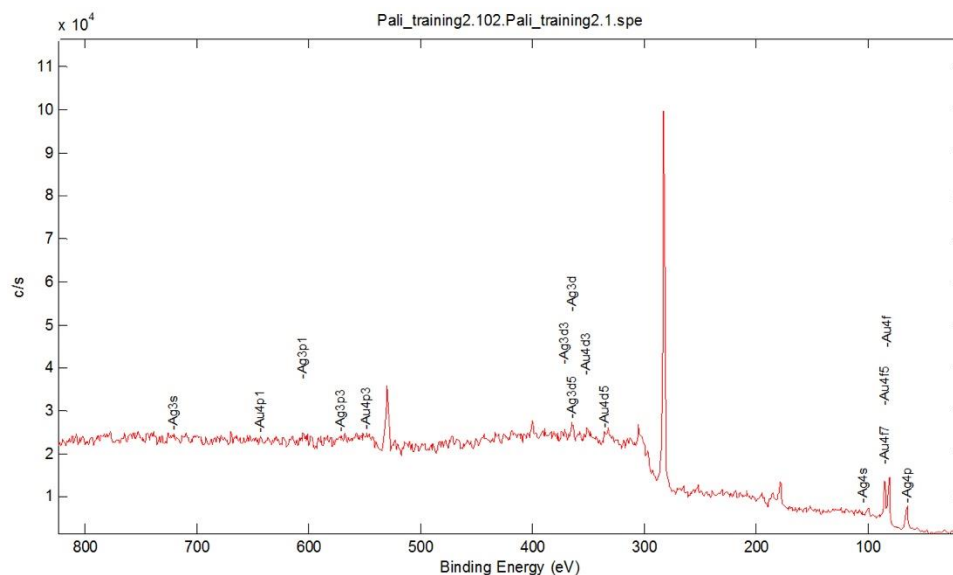


**Figure 4: XPS results showing the presence of silver on gold nanorods.**

Displacement of the stabilizing surfactant CTAB by phospholipid was done in several steps. 1mL of the purchased nanorods were centrifuged at 6000 rpm for 20 min, and the supernatant was discarded. The nanorods were then resuspended in 300  $\mu$ L of 10mg/mL SUVs and lightly sonicated for 20 min. The amount of remaining CTAB was monitored by SERS and the centrifugation and sonication procedure was repeated until the CTAB was no longer detected. Because the quaternary amine of DOPC and DMPC is less charged than the trimethylammonium of CTAB, these alone was not able to stably keep the nanorods suspended in solution. A 10 mol % of DOPG was therefore added to the DOPC and DMPC coated

nanorods to provide extra repulsive charge to keep the nanorods stably suspended in solution.

### 3.3.3. SERS and LSPR Measurements

All SERS measurements presented in this chapter were taken from gold nanorods suspended in solution at room temperature. To control for nanorod concentration, the peak spectral extinction was measured for each sample using an Ocean Optics USB 2000 fiber spectrometer. The excitation source for the SERS experiments was an 80 mW 785 nm diode laser (Ondax), which was then passed through a neutral density filter to reduce the power of the laser to 10 mW at the sample. A 40x/0.5 N.A. near-infrared objective (Olympus) was used both to focus the excitation into the sample cell 10  $\mu\text{m}$  past the front glass window, and also to collect scattered light from the sample and direct it toward the detector. The scattered light was then passed through a notch filter used to further block out any remaining laser signal, and dispersed by an Acton SpectraPro 150 spectrometer, and detected by a Princeton Instruments PIXIS CCD. To ensure the observed Raman signal was in fact surface enhanced from the nanorods in solution, a control spectrum was collected from lipid SUVs in solution without nanorods. The results showed no detectible Raman signal (Figure 5).

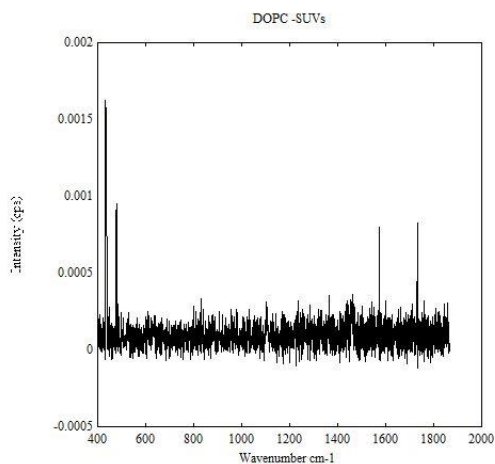


*Figure 5: Raman signal observed from empty lipid vesicles in solution.*

The localized surface plasmon resonance (LSPR) was used to characterize the nanoparticles at room temperature. A 1 cm path length cuvette was used to measure the excitation peak amplitude. Temperature dependent LSPR spectra were collected using a Peltier-controlled cuvette holder from Ocean Optics. Temperature measurements were scanned by increasing the sample temperature at a rate of 0.1 °C/min. Concentration experiments were conducted with slow dilution of the sample by a syringe pump. For these LSPR measurements, the peak excitation wavelength was determined by fitting a Gaussian peak to the LSPR excitation peak. By using this technique and averaging many spectra at each temperature, sub-nanometer shifts in the excitation wavelength can be detected.

### 3.3.4. DLS Measurements

A Malvern Zen 3600 Zetasizer was used for measuring dynamic light scattering (DLS) of the nanorod solutions to characterize their hydrodynamic radius and zeta potential at room temperature. The lipid and CTAB samples were prepared as they were for the SERS and LSPR experiments and at the same concentrations of lipid and surfactant. The nanoparticle concentration for the DLS samples was chosen to match a peak excitation amplitude of 1 in a 1cm path length cuvette. While this concentration of nanoparticles is the same as in the LSPR experiments, it should be noted that for the SERS experiments, the nanorod concentration was increased by 10x.

## 3.4. Results

### 3.4.1. Confirmation of CTAB Exchange

Following the experimental procedure outlined above, SERS spectra were collected at each step in the exchange process and carefully analyzed. The CTAB-stabilized gold nanorod solution gave the spectrum shown in Figure 6. The symmetric stretch of the trimethylammonium headgroup exhibited a peak at 760  $\text{cm}^{-1}$ . Skeletal deformations of the alkane chain correspond to peaks at 1076 and 1148  $\text{cm}^{-1}$ , and peaks at 1273 and 1448  $\text{cm}^{-1}$  correspond to  $\text{CH}_2$  twist and wag vibrations.<sup>30, 53-56</sup> As mentioned before, the  $\text{CTA}^+$  ions of the headgroup is attracted electrostatically to the nanorod surface by the bromide ion which strongly binds to the gold surface.<sup>50, 57</sup> The proximity of the bromide ion to the gold surface

significantly enhances the bromide-gold vibration which was observed at  $176\text{ cm}^{-1}$ .<sup>55</sup> Since silver was observed to be present via XPS analysis,  $\text{AgBr}_2$  may also be present and contributing to the spectra.<sup>58</sup> In a previous study, the bromide ion was replaced with the chloride ion and the peak was shown to shift to  $250\text{ cm}^{-1}$  since chloride is a lighter surface halide.<sup>29</sup>

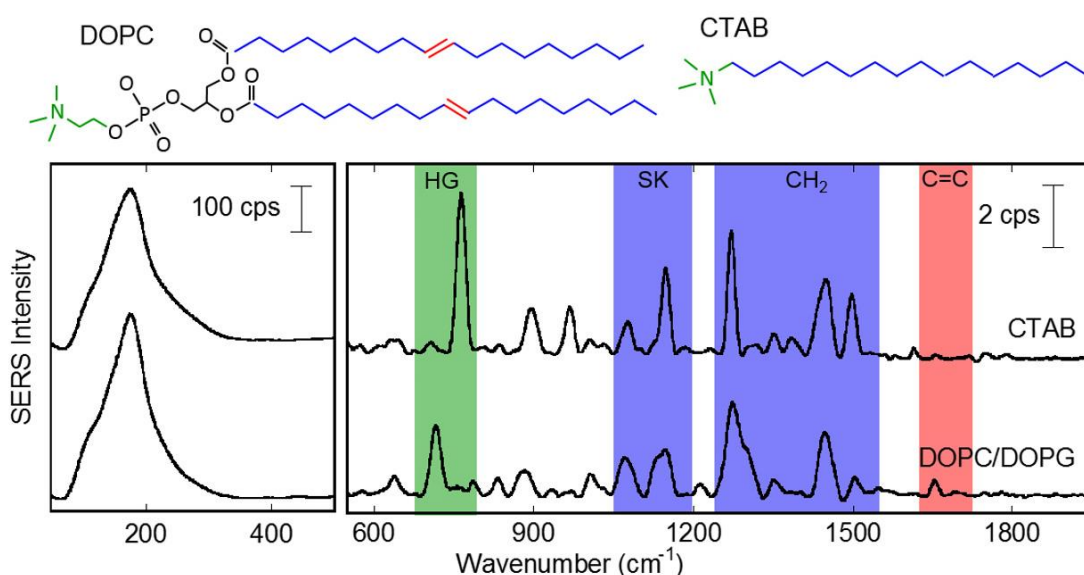


**Figure 6:** The molecular structures of DOPC and CTAB are shown above. The SERS spectra of CTAB and DOPC coated gold nanorods with particular modes highlighted are also shown. Matching colors illustrate vibrational mode locations.

As described in the methods section above, the CTAB stabilized nanorods purchased from Nanopartz were centrifuged and resuspended in solutions of lipid SUVs and bath sonicated. This process was repeated several times and the SERS spectra indicated a significant exchange of CTAB for lipid at the nanorod surface (Figure 6). The DOPC spectra shown in Figure 6 shows a shifted peak at  $718\text{ cm}^{-1}$

which corresponds to the symmetric stretch of the DOPC choline headgroup.<sup>59</sup> The previous CTAB headgroup diminished below detection, however CTAB molecules could still be present in trace amounts at the surface. The data were used to calculate an upper limit on the amount of remaining CTAB at the surface. By integrating the counts between 750 and 775  $\text{cm}^{-1}$  and subtracting a background corresponding to the lowest value, the resulting SERS intensities were 55.2 for the lipid headgroup and 1.9 for the CTAB headgroup (Figure 7). If the surface concentration is proportional to the SERS intensity, the upper limit of residual CTAB is 3% of the total lipid content. We accept this to be considered a full displacement of CTAB by the lipid.

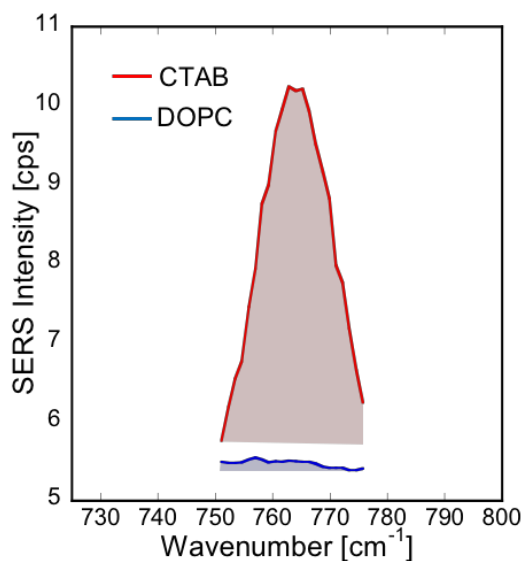


*Figure 7: Area under the curve for the 760  $\text{cm}^{-1}$  headgroup peak of CTAB before (red) and after (blue) exchange with DOPC.*

Analysis of the skeletal peaks (highlighted in blue in Figure 6), the lipid peaks show a broadening compared to the similar CTAB peaks due to the less ordered fatty acid acyl chains of the lipid relative to the CTAB alkane chains. A new peak at  $1655\text{ cm}^{-1}$  corresponds to the double bond of the of the unsaturated chains of the lipids.<sup>54, 59-64</sup> To more fully illustrate the exchange of lipids for CTAB, spectra at intermediate steps were also taken and shown in Figure 8, where the presence of both CTAB and DOPC headgroup peaks can be seen.

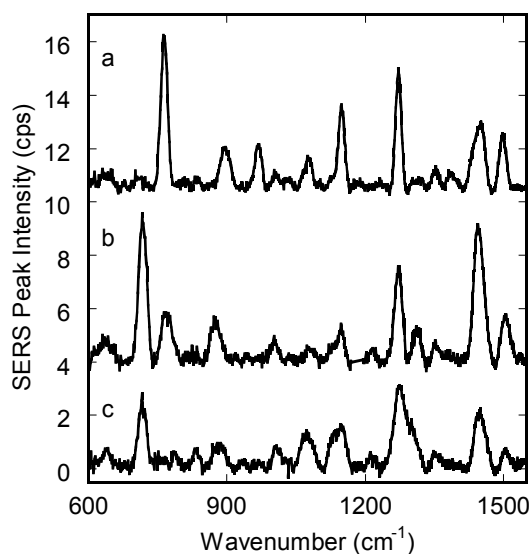


**Figure 8: CTAB to DOPC exchange in three steps: gold nanorod SERS spectra showing the presence of (a) CTAB, (b) mixed CTAB and DOPC, and (c) DOPC.**

### 3.4.2. Nanorod Stability

Exchanging CTAB for DOPC on the surface of the nanorods lowers the surface charge due to the zwitterionic lipid. This has been previously reported and was

confirmed by electrokinetic measurements on the CTAB and DOPC coated nanorods as shown in Table 1.<sup>36, 44, 46</sup>

supporting ligand	zeta potential (mV)
1 mM CTAB	26.7
10 mg/mL DOPC/DOPG	-41.1
2 mg/mL DOPC/DOPG	-16.4

***Table 1: Zeta potential of gold nanorods supported by CTAB and DOPC/DOPG.***

It was observed that when the nanorods are supported solely by DOPC, the nanorods apparently aggregate and a measured loss of the sharp plasmon peak was observed as shown in Figure 9. Others have found that the residual CTAB presence was sufficient to maintain stability of the nanorods in solution, or the use of a charged lipid such as phosphatidylserine was also effective.<sup>36, 39, 44, 46</sup> The inclusion of the anionic DOPG at a 10 % mol ratio with the DOPC was sufficient for our nanorods to stabilize. As seen in Figure 9, after the addition of DOPG, the nanorods become re-stabilized and the sharp plasmon resonance peak is observed. It was also observed that the DOPC coated nanorods could be allowed to aggregate during the exchange with CTAB, and addition of DOPG after apparent aggregation was successful in recovering the well suspended nanorods.



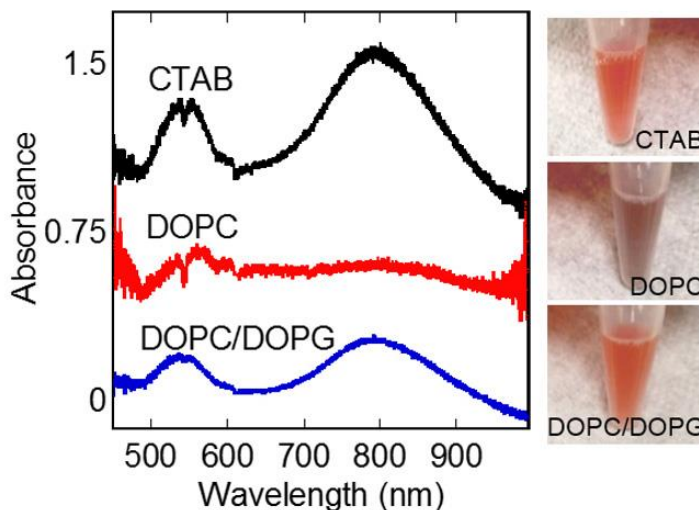


*Figure 9: Extinction spectra and matching photos of gold nanorod samples in CTAB, DOPC, and DOPC/DOPG mixture.*

The reversibility of these aggregated rods suggests that the nanorods remain separated by lipid in the aggregated state, and that the surrounding lipid layers have associated together due to the lack of repulsive charge in the layer. For all other experiments discussed, solutions of a 10 mg/mL DOPC and DOPG 9:1 molar ratio were used to displace CTAB and maintain nanorod stability.

The presence of aggregation with DOPC supported nanorods is troubling since the analysis that will follow requires well separated individual nanorods in solution. The presence of dimers, trimers, or larger aggregates would greatly affect future analysis. For that reason, it is vitally important to confirm as well as possible that the nanorods are not aggregating in solution in a way that could affect the SERS spectra.

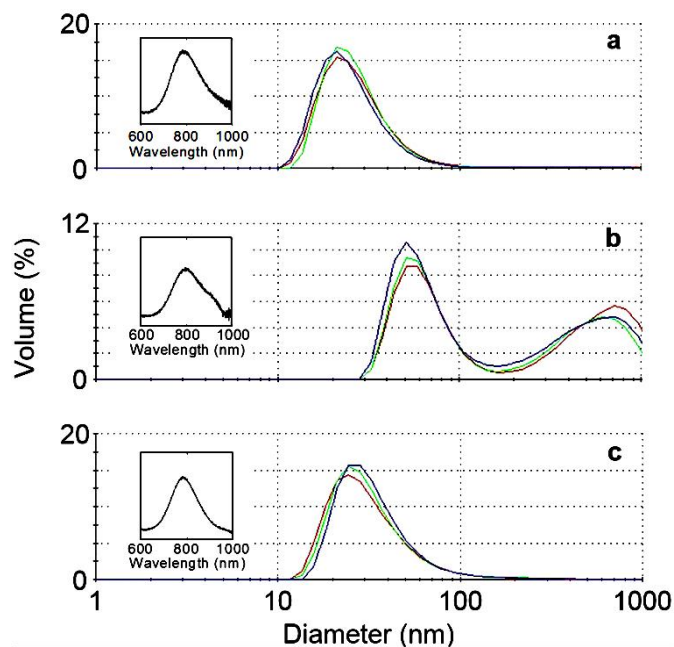


**Figure 10: DLS analysis of gold nanorods supported in (a) 20mM CTAB, (b) 0.7 mM CTAB with ethanol, and (c) 2.5 mM DOPC/DOPG lipids. Insets represent the LSPR spectra for the same sample.**

To some extent the LSPR peak can be used to identify aggregation in samples as shown in Figure 9 with the observation of peak shift and broadening. The polydispersity of the nanorods determines the set line width of these nanorod solutions. In Figure 9 there is no significant spectral broadening when the CTAB surfactant is replaced with DOPC/DOPG lipids. However, a smaller fraction of aggregates could still exist whose presence might not greatly affect the LSPR spectra. Since DLS detects larger nanoparticle aggregates against zero background and the scattering of light by small particles is proportional to the volume of the particle (Equation 2-3), DLS is a very sensitive measurement for aggregation. The stock CTAB stabilized nanorod sample was analyzed by DLS (Figure 10a) and

revealed a single peak. The peak observed shows a size smaller than the nanorod dimension but of the correct order of magnitude expected for single nanorods. The same DLS measurement was performed on CTAB micells and presented a single peak at a size much smaller than the CTAB nanoparticles. It should also be noted that DLS depends on the drift velocity of the particles in solution and therefore provides only the hydrodynamic radius which can be affected by the shape, surface chemistry, surface tension, and other factors. As a control experiment, the CTAB stabilized nanoparticles were made to slightly aggregate by introducing ethanol (Figure 10b) and aggregation is confirmed by the widening of the inset LSPR peak. However, displacement of CTAB with DOPC/DOPG lipids showed no evidence of aggregation down to the limits of detection. This is the best evidence that the SERS signal is coming from well separated nanorods under these conditions.

### 3.4.3. Bilayer Structure and Phase Transitions

As mentioned before, the existence of a well ordered, fluid, natural bilayer is of very high importance for the overall aim of this project. However, showing explicitly that a well formed bilayer exists can be challenging. Examining the SERS spectra for the DOPC/DOPG supported nanorods in Figure 6, several features indicate the lipids are forming a bilayer structure as depicted in Figure 11b,c. It should be noted that the majority of lipid SERS peaks we will mention will be from DOPC since no peaks specific to the DOPG headgroup were detected. The first peak to note is the bromide peak at  $176\text{ cm}^{-1}$ , which remains after the displacement of CTAB by DOPC. The negative bromide ion is used to attract the positive cationic

choline group in DOPC in the same way it attracts the trimethylammonium group of CTAB, and its continued presence supports this claim. Comparing the strength of the headgroup peaks for CTAB and DOPC, the DOPC headgroup is nearly half the strength of the CTAB. However, the peaks for the acyl/alkane chains are of similar strength. This suggests a similar density of hydrophobic tail groups along with a reduction by half in the density of hydrophilic headgroups, which is consistent with the molecular structures of CTAB which contains a single tail per headgroup, and DOPC which contains two tails per headgroup. These observations suggest that the DOPC is binding as expected through the ionic attraction between the terminal choline headgroup of DOPC and the bromide ion on the gold surface. A third observation is that the peak height of the DOPC headgroup at  $718\text{ cm}^{-1}$  is similar in strength to the acyl chain modes for the  $\text{CH}_2$  and  $\text{C}=\text{C}$ . In unenhanced Raman scattering, the acyl chain modes are much stronger than the headgroup mode. In the case of SERS, the electric field enhancement is strongest at the surface of the nanorod and decays rapidly with distance from the surface. Vibrational modes located in a region of higher field enhancement would therefore be enhanced in the SERS spectrum. This alteration to the normal Raman spectrum indicates that the lipids are arranged normal to the gold surface as shown in Figure 11b,c. It should be noted that the field enhancement is observed to be stronger on the ends of the rods than on the sides of the rods, the SERS signal only indicates structure at the ends of the rods.

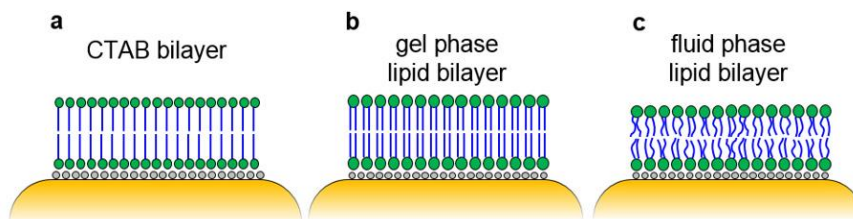


*Figure 11: Illustration of the CTAB bilayer, and gel and fluid phase lipid bilayers.*

Even though analysis of the SERS spectra indicates that the lipids are oriented perpendicular to the gold surface, they do not prove the lipids form a bilayer structure. This is especially true when it is considered that the field enhancement decays so rapidly from the surface of the nanorod that the outer leaf of a supposed bilayer would be expected to provide little or no SERS signal. As in the case of DSC, the phase transition between gel/fluid phases in the acyl chain is a more direct probe of bilayer structure. The transition temperature is sensitive to bilayer composition, and the phase transition temperature has been well characterized by DSC for many lipid membranes.<sup>37, 38</sup> Using calorimetry for our nanorod samples is not practical however, since the quantities of lipids present on the surface of the particles is so small. However, LSPR spectra are routinely taken for our samples and the peak wavelength in LSPR is sensitive to the changing dielectric function of the surrounding medium and is also spatially limited, although not as much as SERS.<sup>14</sup> The structural change between the gel (Figure 11b) and fluid (Figure 11c) phases would alter the environment and should cause a shift in

the LSPR spectra. The shifting peak frequency of LSPR was therefore tracked to detect phase transitions in our samples.

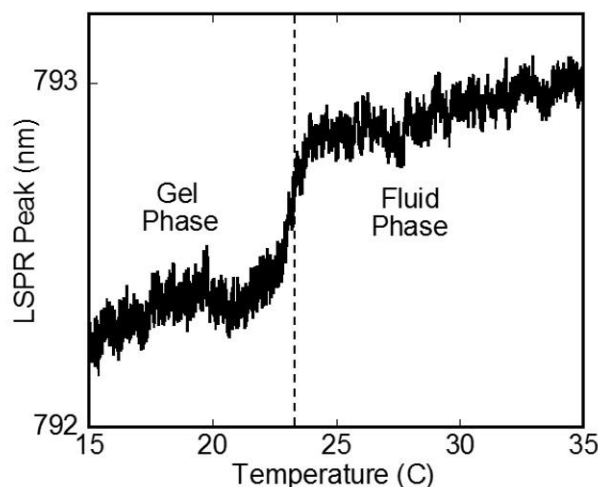


***Figure 12: LSPR peak wavelength vs temperature for DMPC/DOPG supported gold nanorods.***

A lipid layer with an accessible transition temperature is required for such a measurement, so the gold nanorods were prepared with DMPC in the same way as DOPC nanorods, and also stabilized with DOPG as before. The LSPR peak wavelength was tracked as the temperature was slowly ramped at 0.1 °C/min. The LSPR spectra peaks are very broad with a full width half max of 50 nm, the peak center can be accurately tracked by taking many data points. It has been found that the peak wavelength can be tracked with an accuracy of 0.001 nm with a typical excitation value and with 1 minute integration time.<sup>15</sup> In our measurement, the accuracy was around 0.1 nm. Although there was some baseline drift in the

measurement, a sudden jump was detected in the LSPR peak wavelength at 23 °C (Figure 12), which is consistent with the transition temperature of DMPC vesicles as determined by calorimetry.<sup>37, 65, 66</sup> This result strongly indicates that the lipid membranes on the nanorods resemble the structure of the lipid bilayers widely studied in the form of empty vesicles and biomembranes.

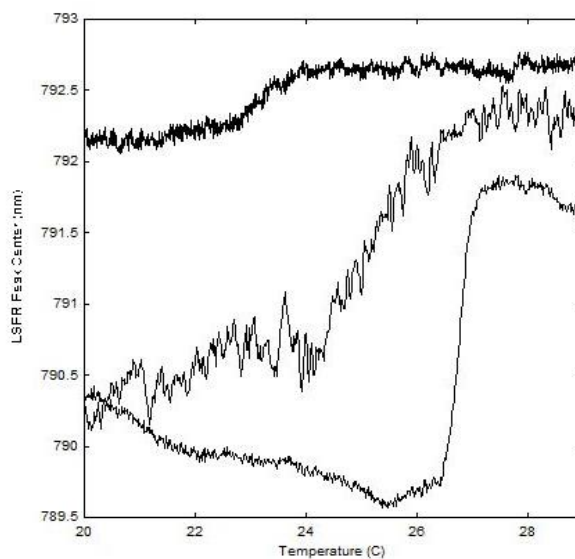


*Figure 13: Three temperature scans of DMPC/DOPG showing the phase transition. Top scan is from Figure 12, and the bottom scan is from Figure 16d*

#### 3.4.4. Bilayer Exchange

While we have now shown that the lipids form well-ordered bilayers on the surface of nanoparticles through the bromide ion electrostatic attraction mechanism observed in CTAB, the strength of this ionic attraction to the gold has not been characterized. For a supported membrane to behave naturally, it must be loosely bound to the surface and must exchange freely with lipids in solution. To

investigate these properties, the lipid exchange between DOPC/DOPG bilayers and the deuterated variant DOPC-d<sub>9</sub> was monitored by SERS. The deuteration of the DOPC-d<sub>9</sub> lipid is limited to the choline methyl groups, and shifts the DOPC headgroup mode from 718 cm<sup>-1</sup> to 640 cm<sup>-1</sup>. DOPC/DOPG supported nanorods were diluted with DOPC-d<sub>9</sub>/DOPG to make a 1:1 mixture of DOPC and DOPC-d<sub>9</sub> while maintaining stability with DOPG. The SERS spectra in Figure 14 shows the initial SERS spectra and the SERS spectra after a short time showing that the DOPC-d<sub>9</sub> had completely exchanged since the choline group peaks are approximately equal in amplitude, matching the equal concentrations.

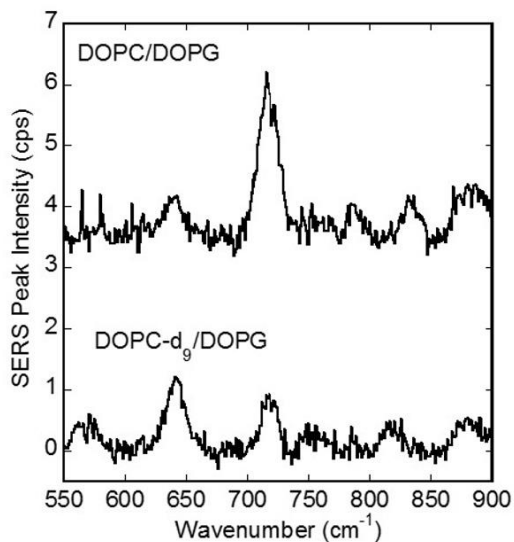


***Figure 14: Initial and final SERS spectra of DOPC/DOPG supported nanorods incubated with deuterated DOPC-d<sub>9</sub> vesicles at a 50 mol %.***

Complete exchange takes 1-2 hrs which is in good agreement with kinetic studies of lipid exchange with vesicles, nanoparticles, and flat surfaces.<sup>42, 67-69</sup> While



Figure 14 shows the initial and final results, the full kinetics can be seen in Figure 15.

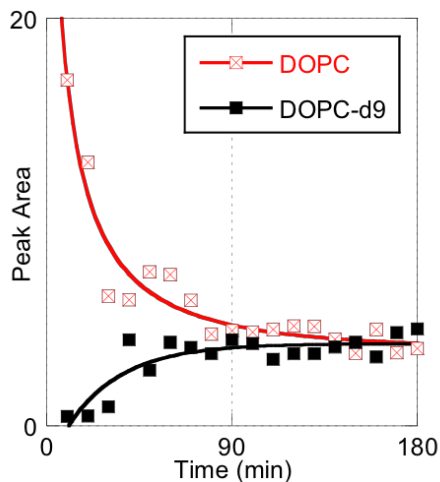


*Figure 15: Full kinetic rate curves for the adsorption of DOPC-d<sub>9</sub> into the formed DOPC lipid layer on gold nanorods.*

### 3.4.5. Bilayer Stability

It is well known that for CTAB stabilization of nanorods, a minimum concentration of CTAB is required.<sup>29, 50</sup> Since lipid exchange with solution was easily verified above, it follows logically that lipid stabilization of gold nanorods may have similar limitations. Several reports have shown however that lipid coated nanorods can remain stable in solution even in the absence of lipid vesicles.<sup>44, 46</sup> To explore the stability if the lipid bilayer in solution, DOPC/DOPG stabilized nanorods were diluted from 10 to 0.001 mg/mL through four rounds of centrifugation and resuspension into DI water. Examining the LSPR plasmon peak before and after dilution revealed no significant change. SERS spectra were also collected before and

after dilution and revealed a very stark change in the relative peak strength between the acyl chain modes and the headgroup mode as seen in Figure 16a. A similar transition has been observed in CTAB and could indicate a restructuring of the bilayer on the surface of the nanoparticle from a bilayer to a collapsed or disordered state where the acyl chains are closer to the nanorod.<sup>29</sup> Further evidence for this structural shift can be seen by tracking the LSPR peak wavelength as the lipid supported nanorods are diluted (Figure 16b). Similar to the results for the phase transition, a sudden shift was detected near 0.9 mg/mL DOPC/DOPG, which could be due to a change in the conformation of the bilayer.

To verify the loss in the bilayer structure, DMPC/DOPG supported gold nanorods were prepared and lipids were diluted from 10 to 0.006 mg/mL to achieve a disordered state as observed by SERS (Figure 16c). Additionally, LSPR temperature scans were performed before and after the dilution, and a gel/fluid phase transition was observed but only for the sample at the high concentration of vesicles in solution (Figure 16d).

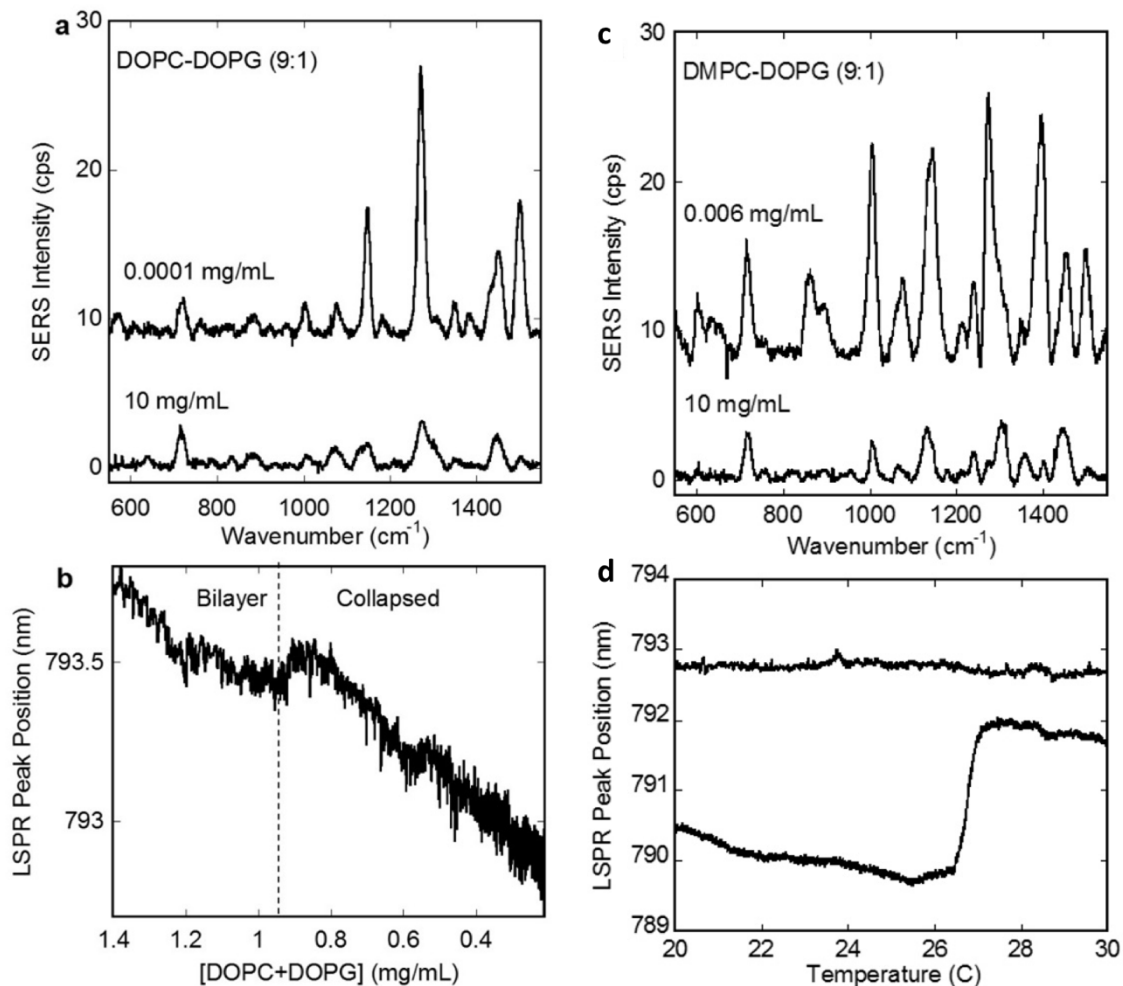


**Figure 16: Lipid layer structural transitions. a) SERS spectra of DOPC/DOPG supported gold nanorods at 10mg/mL and 0.001 mg/mL concentrations. b) LSPR peak wavelength of DOPC/DOPG lipids during dilution from 1.4 to 0.2 mg/mL concentration. c) SERS of DMPC/DOPG coated nanorods at 10 mg/mL and 0.006 mg/mL concentrations. d) LSPR peak wavelength of DMPC/DOPG coated nanorods. A bilayer transition is only shown in the higher concentration (bottom), and no transition for the lower concentration (top).**

The low concentration sample showed no sign of phase transition and is therefore unlikely to be in a lipid bilayer structure. While a collapse to a non-bilayer state is well-known for surfactants,<sup>70</sup> lipids could be expected to form more stable

structures given their propensity for forming stable bilayer structures. However, lipids do tend to behave like surfactants in the case of lipid coatings on nanoparticles, and the interaction between the lipid and the nanoparticle surface must be considered. It is our suspicion that the attraction of the lipid to the gold surface is responsible for the transition to the disordered state and explains how even in very low lipid vesicle concentration, the nanoparticles can escape aggregation.

Exploring the effects of low concentration lipid vesicles on the lipid structures for nanorod supported membranes is subject to effects of aggregation. For this reason, DLS and LSPR analyses were performed on gold nanorod samples of decreasing lipid vesicle concentration. These results are shown in Figure 17. As previously reported, the LSPR spectra remains unchanged with lowering concentration.<sup>44, 46</sup> The more sensitive DLS measurements do show a clear sign that a small fraction of the nanoparticles is aggregating at low lipid concentration (Figure 17). It is unclear if these particles are fusing permanently or loosely as in the flocculated state shown in Figure 9b. Even though DLS indicates these aggregated rods make up a minority of the sample, the increased SERS signal due to plasmonic hot spots could be dominating the SERS signal. In this case, a simple enhancement decay argument cannot be made for interpreting structure as before. The increased acyl chain SERS signal observed above could be due to the enhanced field of two nanoparticles in close proximity to one another and sharing a single lipid bilayer. Although SERS cannot indicate the structure due to potential aggregation, the LSPR peak wavelength measurements in Figure 16b,d are not

affected by aggregates and directly indicate a transition where the bilayer structure is lost.

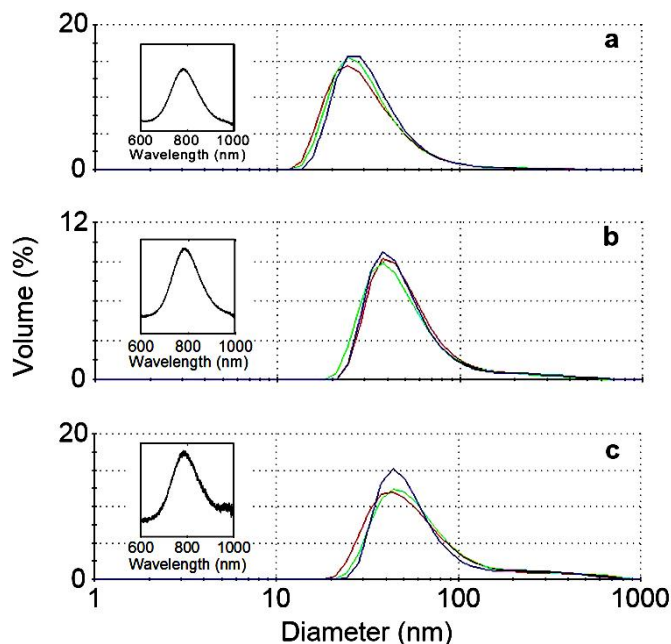


**Figure 17: Dynamic light scattering of gold nanorods supported with DOPC/DOPG at a) 1, b) 0.1, and c) 0.01 mg/mL concentrations. Matching LSPR curves for each sample are shown as insets.**

The observation of a non-bilayer state and the lipid gold interface described here both yield possible insights for nanomedicine. Gold nanoparticles have been developed for diagnostic and therapeutic applications because of their strong optical scattering, near field enhancement, and resonant heating.<sup>71-73</sup> While many of these utilize antibodies, surface bound polymers, or nucleic acids for targeting and circulation, the use of lipid membrane coatings is under development.<sup>34-36, 39-49</sup> The assays used to characterize lipid conjugated nanoparticles detects nanoparticle stability and lipid presence, but does not carefully characterize bilayer structure.

Transferring lipid stabilized particles into a clean buffer could cause the kind of structural transition observed in Figure 16. This could have a significant impact on the interactions between these nanoparticles and cells or analytes that interact with membrane receptors. SERS provides a simple diagnostic that could be used to characterize the bilayer state or possible aggregation by comparing acyl chain and phosphatidylcholine headgroup vibrational modes. Additionally, such analysis could benefit studies on how surfactants stabilize and passivate nanoparticles, which is not fully understood.<sup>29, 46</sup>

## Chapter 4

# SABERS

“The way to have good ideas is to have lots of ideas, and throw away the bad ones.” – Linus Pauling

### 4.1. Analytical SERS

Surface enhanced Raman scattering (SERS) serves as a powerful tool for the analysis of interfacial molecular structure.<sup>29, 34, 74, 75</sup> The vibrational spectra provides specificity without the use of molecular labels, the near field enhancement decays rapidly over length scales of molecules, and the enhanced field is also aligned perpendicular to the metallic surface providing selectivity in vibrational modes as we shall demonstrate. Added benefits to SERS are that experiments can be conducted in ambient conditions in solution, and only microscopic quantities of materials are needed per experiment. The difficulty lies in interpreting the SERS signal itself due to the complex structure of the electromagnetic near field,

complicated polarizability and vibrational modes of large molecules of interest, variations of orientations and positions of molecules relative to the nanorod surface, and possible interactions between the metallic surface and the molecules themselves.<sup>19, 76-78</sup> If these effects were understood and accounted for, experimental SERS measurements would unveil detailed molecular structures of value to fields such as interfacial chemistry, catalysis, and structural biology.

In this chapter, the framework for structural analysis by enhanced Raman scattering (SABERS) will be laid, and in Chapter 5 SABERS will be applied toward probing the DTAB surfactant layer and the orientation and position of tryptophan in lipid membranes on the surface of a gold nanorod. SABERS combines experimental SERS and Raman spectra with polarizability tensors calculated from time dependent density functional theory (TDDFT) and electromagnetic near fields from numerical simulations with finite element analysis (FEA), to determine the position and orientation of specific molecules near the surface of a nanorod (Figure 18).



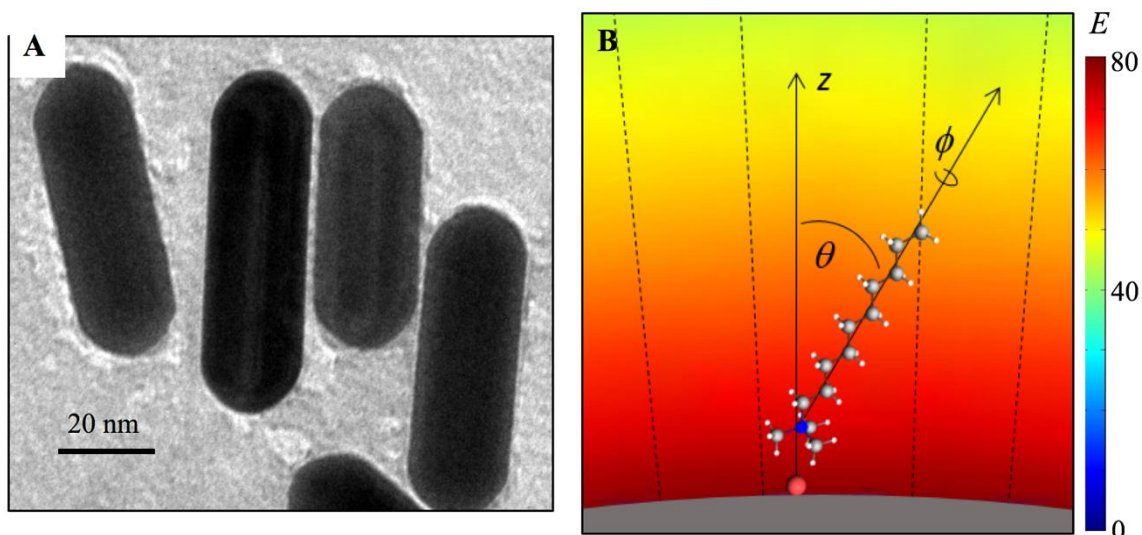


**Figure 18: The gold nanorod nearfield optics of SABERS. A) A transmission electron micrograph of the gold nanorods used in the study that have 25nm diameter hemispherical endcaps. B) A scaled overlay of the calculated electric field lines (dashed) and the electric field magnitude (color scale) from an EM simulation, and the TDDFT optimized structure of DTAB on the tip of the nanorod (gray). The coordinate system for the orientation is also presented.**

## 4.2. Predicting Structure

### 4.2.1. Raman and SERS Calculation

The structural analysis in SABERS requires both experimental SERS and Raman and also theoretical Raman spectra. The experimental procedures for the SERS and Raman data are outlined in Chapter 5, but here we describe the calculation of the predicted signals. We begin with an expression for the unenhanced Raman scattering for the classical treatment of Raman scattering for randomly oriented molecules given as:<sup>79</sup>

$$I(\pi/2) = k_\nu N(\nu_0 - \nu_n)^4 \left\{ \frac{45(a'_n)^2 + 7(\gamma'_n)^2}{45} \right\} Q_{n0}^2 I_0$$

where  $k_\nu$  is just a combination of parameters:  $k_\nu = \pi^2/\epsilon_0^2$ .  $N$  is the number of molecules.  $\nu_0$  and  $\nu_n$  are wavenumbers of the incident and Raman shifted light (defined without the  $2\pi$ ),  $Q_{n0}$  is the normal mode amplitude, and  $I_0$  is the excitation power from the laser. The mean derived polarizability  $a'$  and the anisotropy  $\gamma'$  invariants follow the standard definition:

$$a' = \frac{1}{3}(\alpha_{xx} + \alpha_{yy} + \alpha_{zz})$$

$$\gamma'^2 = \frac{1}{2} \left( (\alpha_{xx} - \alpha_{yy})^2 + (\alpha_{yy} - \alpha_{zz})^2 + (\alpha_{zz} - \alpha_{xx})^2 + 6(\alpha_{xy}^2 + \alpha_{yz}^2 + \alpha_{zx}^2) \right)$$

***Equation 4-1: Polarizability and anisotropy invariants definitions.***

For a semi-quantum treatment, the normal mode amplitudes are replaced by a Boltzmann factor to represent the relative population of states (among other things):

$$I(\pi/2) = k_\nu N(\nu_0 - \nu_n)^4 \left\{ \frac{45(a'_n)^2 + 7(\gamma'_n)^2}{45} \right\} \frac{h}{8\pi^2 c \nu_n (1 - e^{-h c \nu_n / k_B T})} I_0$$

where everything is defined as before and  $h$  is Planck's constant,  $c$  is the speed of light,  $k_B$  is Boltzmann's constant, and  $T$  is temperature.

Here it is in somewhat more modern notation, using angular frequency rather than wavenumber:

$$I(\pi/2) = \frac{N}{32\pi^2 c^4 \epsilon_0^2} \frac{(\omega_0 - \omega_n)^4}{\omega_n} \left\{ \frac{45(a')_n^2 + 7(\gamma')_n^2}{45} \right\} \frac{1}{(1 - e^{-\omega_n/k_B T})} I_0$$

We can therefore write our Raman count rate as:

$$I(\pi/2) = kN_{Raman} \frac{(\omega_0 - \omega_n)^4}{\omega_n} \left\{ \frac{45(a')_n^2 + 7(\gamma')_n^2}{45} \right\} \frac{1}{(1 - e^{-\omega_n/k_B T})} I_0$$

Where  $k$  includes the constants as well as factors related to our optical setup,  $\omega_0$  is the excitation frequency and  $\omega_n$  is the Raman shifted frequency for the  $n^{th}$  normal mode, and  $N_{Raman}$  is the number of molecules in the beam spot. This expression is for backscattered light and is independent of scattered polarization in order to match our experimental setup.

For the SERS signal,  $I_{SERS}$ , we can modify the Raman count rate with the electromagnetic enhancement and Raman tensor components relevant to each normal mode. This assumes that the molecules do not strongly interact with the nanoparticle surface which is a valid approximation since in our experiments the surfactant and lipid molecules bind electrostatically with the bromide ion, and tryptophan is only inserted into the lipid bilayer. Therefore, we write our SERS count rate as:

$$I_{SERS} = kN_{SERS} \frac{(\omega_0 - \omega_n)^4}{\omega_n} E_{n,0}^2 E_{n,R}^2 \alpha_{zz}^2 \frac{1}{(1 - e^{-\omega_n/k_B T})} I_0$$

*Equation 4-2: The expression for the computed SERS count rate.*

Where we have replaced the space averaged combination of tensor terms with  $\alpha_{zz}$ , and included the field enhancements.  $N_{SERS}$  is the number of molecules at the nanorod end in the focused beam spot,  $\alpha_{zz}$  is the relevant component of the Raman tensor since the E-field at the nanorod end remains perpendicular to the nanorod surface regardless of nanorod orientation in the polarized beam, and we define the normal at the nanorod end to be in the  $\hat{z}$  direction.  $E_{n0}$  and  $E_{nR}$  are the field enhancements at the excitation and Raman shifted wavelengths, respectively, for the  $n^{th}$  vibrational mode. These factors are specific to each mode since different vibrations occur at different locations in the spatial and frequency decays of the field enhancement, specified by the center of vibration position from the nanoparticle surface and the vibration frequency shift from the excitation frequency. The center of vibration for each normal mode is determined by us from the average position ( $r_m$ ) and vibrational amplitude ( $A_m$ ) of each atom to identify the center of vibration by the following formula:

$$C_n = \frac{\sum_m A_m r_m}{\sum_m A_m}$$

Where  $C_n$  is the position of the center of vibration for the  $n^{th}$  vibrational mode. The z-component for each normal mode is used at the location in the near field to find its enhancement values. Sample centers of vibration are given in Figure 20 and Figure 23.

### 4.2.2. Electric Field Enhancement

The norm of the electric field at the surface of the nanoparticle along the axis normal to the surface (as in Figure 18) was read from the result of the COMSOL simulation (details in 5.2.4) at the excitation and further red shifted frequencies. The two-dimensional data set was found to decay exponentially with both position from the nanorod surface and frequency shift from the resonant peak excitation frequency, so it was fit to the following function of wavelength shift ( $\lambda$ ) and position ( $z$ ):

$$E_{norm} = (a + b\lambda + cz) + de^{(f\lambda + gz)}$$

***Equation 4-3: Generalized form of the exponential electric field enhancement as a function of wavelength shift and z-position.***

For example, Figure 19 shows the electric field norms as calculated in COMSOL and fitted with the above expression. The field norms are shown as a function of z-position at the two excitation wavelengths 785 nm, and the shifted wavelength corresponding to 718  $\text{cm}^{-1}$  which is the frequency of the symmetric choline stretch in DOPC. The fit parameters were likewise used to calculate the enhancement factors  $E_{n,0}$  and  $E_{n,R}$  for each mode based on its frequency shift and center of vibration z-position.

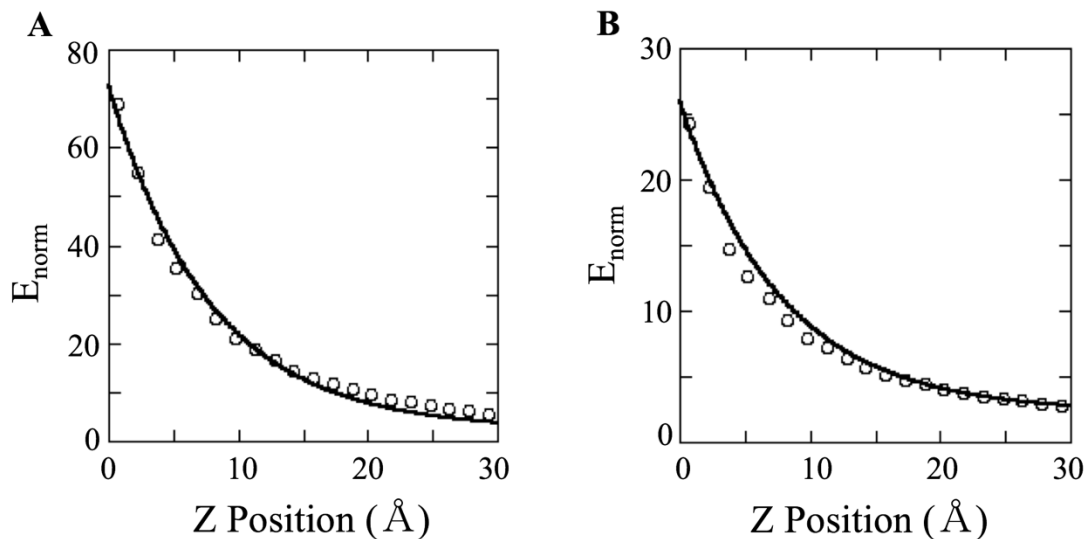


*Figure 19: The electric field norm as a function of distance from the nanorod surface at A) 785 nm excitation wavelength, and B) an excitation wavelength corresponding to the 718 cm<sup>-1</sup> symmetric stretch of the DOPC headgroup.*

#### 4.2.3. Comparison with Experiment

The instrument parameters contained in the constant  $k$  in Equation 2-2 are difficult to characterize. If we divide the measured SERS peak heights (in cps) by the corresponding measured Raman peak heights (cps), the resulting ratio  $r_n$  is independent of these factors, if differences in excitation power and integration time are taken into account. The ratio  $r_n$  is then defined as follows:

$$r_n = \frac{I_{SERS}}{I_{Raman}} = \frac{N_{SERS} E_{n,0}^2 E_{n,R}^2}{N_{Raman}} \frac{\alpha_{zz}^2}{\left\{ \frac{45(a'_n)^2 + 7(\gamma'_n)^2}{45} \right\}}$$

Although several factors are cancelled in the calculation of  $r_n$ , it is still sensitive to the number of molecules probed, which is also difficult to characterize. We therefore calculate a second ratio  $R_{1-2}$  which is the relative height of two peaks within the spectrum.

$$R_{1-2} = \frac{r_1}{r_2} = \frac{E_{1,0}^2 E_{1,R}^2 \alpha_{zz,1}^2 \{45a_2^2 + 7\gamma_2^2\}}{E_{2,0}^2 E_{2,R}^2 \alpha_{zz,2}^2 \{45a_1^2 + 7\gamma_1^2\}}$$

This ratio only depends on the position and orientation of the molecule relative to the surface of the nanoparticle through terms we can calculate by EM simulations and TDDFT.

To go one step further, if we consider the equation for  $r_n$  with the understanding that the ratio  $R_{1-2}$  will be taken later so that we can ignore the cancelable factors, the calculation can be taken to higher order by considering not only the polarizability tensor  $\alpha_{zz}$ , but also the dipole-quadrupole term  $A_{zzz}$  also calculated from the TDDFT simulation. Inclusion of this term changes the enhancement term in the  $r_n$  ratio from

$$r_n \approx E_{n,0}^2 E_{n,R}^2 \frac{\alpha_{zz}^2}{\left\{ \frac{45(a'_n)^2 + 7(\gamma'_n)^2}{45} \right\}}$$

to the more complicated form of

$$r_n \approx \left( \begin{array}{l} E_{k,0}^2 E_{k,R}^2 \frac{\alpha_{zz}^2}{\left\{ \frac{45(a')_n^2 + 7(\gamma')_n^2}{45} \right\}} + \frac{1}{9} \nabla \cdot E_{k,0}^2 \nabla \cdot E_{k,R}^2 A_{zzz}^2 \dots \\ - \frac{2}{3} E_{k,0} E_{k,R} \nabla \cdot E_{k,0} \nabla \cdot E_{k,R} \frac{\alpha_{zz} A_{zzz}}{\left\{ \frac{45(a')_n^2 + 7(\gamma')_n^2}{45} \right\}^{\frac{1}{2}}} \end{array} \right)$$

This higher order expression takes more careful consideration of the rapidly changing field enhancement near the surface of the nanorod by also including gradient field effects.

The molecular orientation and position are determined by calculating the ratio  $R_{1-2}$  for varying angles and positions, and comparing the values to the experimental versions of the same ratio by calculating the similarity as defined in Equation 4-4. The product and  $n^{th}$  root handle situations where multiple peak ratio similarities are calculated such as in the case of tryptophan where multiple peaks are compared and a single similarity must be computed between theory and experiment.

$$Similarity = \left( \prod_n \left( 1 - \frac{|R_{exp,n} - R_{ADF,n}|}{R_{exp,n} + R_{ADF,n}} \right) \right)^{\frac{1}{n}}$$

***Equation 4-4: The definition of Similarity used in comparing the theoretical and experimental peak ratios.***



# **Tryptophan and DTAB Positions and Orientations in Gold Nanorod Supported Membranes**

“One good test is worth a thousand expert opinions.” – Wernher Von Braun

### **5.1. Introduction**

Having developed the framework of lipid membranes on gold nanorods, and the theory of utilizing the unique field enhancement of the surface plasmon on the nanorod for deducing molecular arrangements at the nanoparticle’s surface, now consider two examples of application for this method. The first example is the

orientation of CTAB at the surface of the nanorod, and the second is the orientation and position of Tryptophan adsorbed into nanorod supported lipid membranes. As these two examples are considered, understand that the data analyzed here is similar to the SERS spectra presented before. The spectra themselves contain no new information from typical SERS spectra such as those presented in earlier chapters. But by examining this data through the newly formed filter of SABERS analysis, new insight is obtained which can be further applied to many such examples.

## **5.2. Methods and Materials**

### **5.2.1. Materials**

Once again, the lipids 1,2-dioleoyl-sn-glycero-3-phospholipid (DOPC), 1,2-dioleoyl-sn-glycero-3-phospho-(1'-rac-glycerol) (DOPG) were purchased from Avanti in chloroform solution. L-tryptophan (Sigma Aldrich) and the surfactant decyltrimethylammonium bromide (DTAB, Fluka #30725) were also purchased. Gold nanorods suspended in cetyltrimethylammonium bromide (CTAB) with nominal 25 nm diameter, 100 nm length, and 780 nm localized surface plasmon resonance peak wavelength were purchased from Nanopartz.

### **5.2.2. Sample Preparation**

Replacing the stabilizing surfactant CTAB with the surfactant DTAB at the surface of the nanorods was accomplished by taking a 1 mL volume of the

purchased nanorod solution and centrifuging the nanorods at 5,800 rcf (6,000 rpm) for 20 min, removing the supernatant, and resuspending the nanorods in 5 mM DTAB. This process was repeated 3 times, after which the LSPR spectra were analyzed to verify the nanorods remained well separated and stabilized in solution.

To replace the native CTAB surfactant with lipid, the same procedure outlined in 3.3.2 was used. As before, a 9:1 lipid mixture of DOPC:DOPG was used in order to stabilize the nanoparticles in solution. The lipids were dried from chloroform and hydrated with DI water to bring the concentration to 10 mg/mL. The hydrated multilamellar vesicles were then bath sonicated until the formation of single lamellar vesicles (SUVs) was observed. Gold nanorods were pelleted and resuspended in the lipid solution and then sonicated in a water bath for 20 min. This process was also repeated 3 times until the displacement of CTAB by lipid was verified with SERS.<sup>74</sup> For the tryptophan analysis, tryptophan was added to the lipid stabilized nanorod solution at a mole fraction of 1/6, tryptophan/lipid concentration.

Unenhanced Raman spectra of DTAB was taken from micelles in solution. For the lipid and tryptophan mixture, Raman of SUV's in solution was too weak to provide a usable spectrum, so the material was lyophilized and the spectra were recorded from the powder under ambient conditions. The mole ratio for the unenhanced Raman spectrum was always the same as in the corresponding SERS measurement.

### 5.2.3. Raman Spectrometer

The spectra were all collected from the same equipment outlined in 3.3.3. A custom Raman microspectrometer optimized for near infrared wavelengths was used for the Raman and SERS measurements. The excitation source was a 80 mW, 785 nm, temperature controlled, wavelength stabilized diode laser. The laser was further filtered by a volume holographic grating (Ondax). The beam is then passed through a variable neutral density filter to reduce the power to 10 mW at the sample. A 100x/0.85 IR LCPlan N Olympus objective is used to both focus the laser onto the sample and to collect scattered and direct light from the sample to the spectrometer. A second 5x/0.1 IR LMPlan N Olympus objective then focuses the directed scattered signal into the entrance slit of an IsoPlane SCT320 spectrometer from Princeton Instruments. The improved ability for this spectrometer to resolve accurate peak heights is due in large part to the low astigmatism compared to a traditional Czerny-Turner design. The detector is a front illuminated, open electrode PIXIS 256 CCD (Princeton Instruments). Liquid samples were drawn into thin glass capillary tubes that are 2 mm wide and 0.1 mm in depth, and the primary objective was set to focus 30  $\mu\text{m}$  into the sample from the front glass wall.

### 5.2.4. Electromagnetic Simulations

Near field calculations of the gold nanorods were performed by electromagnetic simulations run in COMSOL Multiphysics using the RF module. A gold nanorod corresponding to the size and aspect ratio of the nanorods used in our experiment was constructed and a surrounding medium corresponding to water

was implemented and surrounded by a perfectly matching layer (PML). The classic Johnson and Christy dielectric data were used for calculation of the extinction cross section for incoming light with the electric field polarized along the nanorod length with the wave vector transverse to the nanorod.<sup>80</sup>

### 5.2.5. TDDFT Calculations

Raman tensors for the molecules were calculated by time dependent density functional theory TDDFT.<sup>81</sup> The TDDFT calculations were carried out using Amsterdam Density Functional program from Software for Chemistry & Materials. The molecular arrangements shown in Figure 20 and Figure 23 were constructed and their geometries were optimized using the Becke-Perdew exchange correlation potential under the generalized gradient approximation (GGA-BP) with a triple zeta basis set with one polarization function (TZP), a large frozen core, and scalar ZORA relativistic correction. The numeric quality was set to “good”. Once the geometry was optimized, the vibrational Raman optical activity (VROA) calculation was carried out for 785 nm excitation with numerical frequencies and two-point numerical differentiation to find the polarizability tensor  $\alpha$ .

### 5.2.6. Ratio and Similarity Calculations

The experimental Raman and SERS spectra were collected and analyzed with a MATLAB script that subtracts background, plots the spectra and determines the peak height and full width at half maxima (FWHM). Since the experimental peaks have varying width, the peak area for each peak was calculated by multiplying the

peak height with the FWHM. The peak areas were then used to calculate the experimental ratios  $r_n$ . The theoretical Ratios were computed from the Raman tensor components taken directly from the output of the TDDFT calculation. The theoretical peaks were assumed to all have the same FWHM so that calculation of the theoretical ratios  $r_n$  removed any FWHM effect. Sample ratio values are provided in Table 2 and Table 3.

The similarity defined in REF was calculated as a function of orientation and z-position. Rotations of the molecules were treated as rotations of the DFT tensors and rotation and translation of the (x, y, z) position of the center of vibration for each mode. Initially the molecule was rotated and translated to an initial position with a defined axis of molecular alignment normal to the gold surface (the z-axis normal to the gold surface). For each subsequent rotation away from the initial position, the DFT tensor was rotated using the rotation matrix defined by the  $\theta$  and  $\phi$  angles. The electric field in the x-y plane was assumed to be uniform over an area of radius equal to the length scale of a single molecule so that rotations around the third angle  $\psi$  were irrelevant. The  $\alpha_{zz}$  tensor component was used to determine SERS intensities and the rotation invariant  $45(a)^2 + 7(\gamma)^2$  was used to calculate Raman intensities for the particular orientation. The mean derived polarizability ( $a$ ) and the anisotropy ( $\gamma$ ) invariants follow the standard definition give in REF.

The z-positions of the molecules were also varied, which affected the calculation through the enhancement factors. The tensor components and enhancement factors were combined in REF to find the calculated ratios for all

positions and orientations. These results were then compared to the experimental ratios and the similarity between  $R_{exp}$  and  $R_{TDDFT}$  was calculated as expressed in REF.

### 5.3. DTAB Orientation

As an application of the technique outlined above, the orientation of the stabilizing surfactant decyltrimethylammonium bromide (DTAB) is considered. SERS spectra were recorded from surfactant-stabilized gold nanorods freely diffusing in solution. For this geometry, SERS is observed from isolated nanorods in solution with electromagnetic enhancements on the order of  $10^5$  at the nanorod ends.<sup>29, 75</sup> Even though fields of larger enhancements can be produced in hot spots between two or more nanoparticles, isolated particles provide reproducible enhancement fields more amenable to characterization.<sup>28</sup>

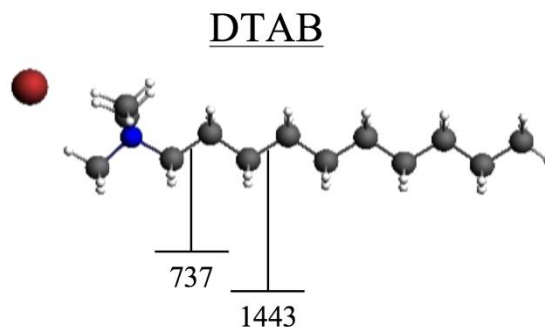


***Figure 20: TDDFT optimized structure of decyltrimethylammonium bromide (DTAB). Numerical labels indicate the positions and wavenumbers ( $\text{cm}^{-1}$ ) of the centers of vibration.***

The SERS, Raman, and TDDFT calculated spectra for the stabilizing surfactant DTAB are shown in Figure 21A. DTAB stabilized nanorods were used to generate the SERS spectrum, and the unenhanced Raman spectrum was taken from DTAB micelles in solution at the same concentration as the DTAB stabilized nanorods. The TDDFT spectrum is taken from the orientation averaged Raman signal based on the tensor invariants expression in REF. Two modes are clearly identified in all three spectra: the symmetric stretch of the headgroup at  $773\text{ cm}^{-1}$  and the  $\text{CH}_2$  scissor mode at  $1457\text{ cm}^{-1}$ . The experimental ratio values  $r_N$  and  $R_{1-2}$  as defined in REF were calculated as the SERS to Raman ratio ( $r_{N(\text{Exp})}$ ) and the peak to peak ratio ( $R_{1-2(\text{Exp})}$ ) within the spectrum. The theoretical ratio  $R_{1-2(\text{DFT})}$  is similarly calculated from the TDDFT determined polarizability tensor  $\alpha$  at a particular orientation and then compared to the experimental ratio  $R_{1-2(\text{Exp})}$  using the Similarity as defined in Equation 4-4. This Similarity index was calculated for all angles and plotted in Figure 21B.



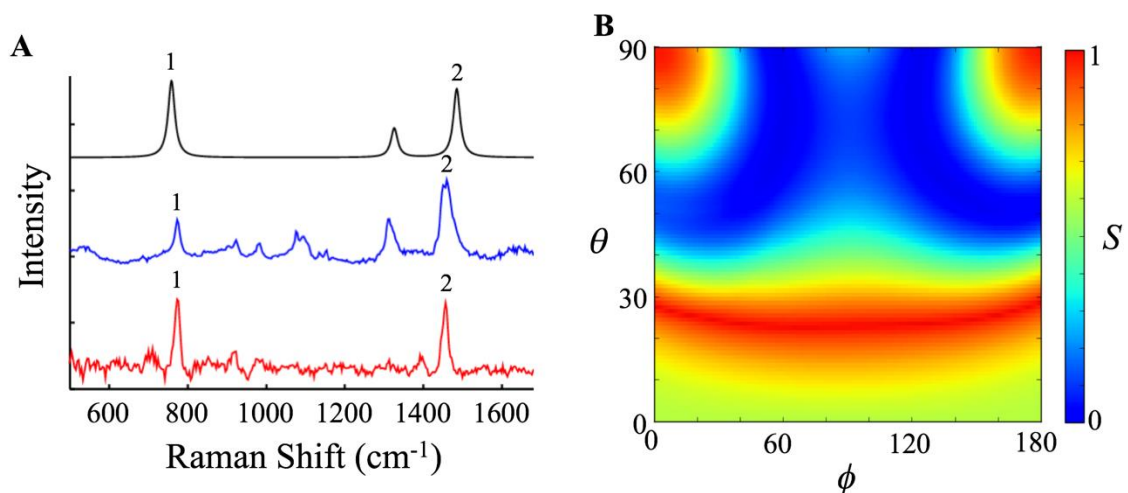


**Figure 21: The DTAB surfactant structure according to SABERS. A) The SERS spectrum of DTAB on gold nanorods (red), the Raman spectrum of DTAB micells (blue) and the TDDFT spectrum for DTAB. The two peaks used for the calculation of  $R_{1-2}$  are labeled. B) The similarity  $S$  between theory and experiment for all accessible angles  $\theta$ ,  $\phi$ . The high band at  $\theta = 25^\circ$  and independent of  $\phi$  represents a tilted bilayer structure.**

The results of the Similarity calculation indicate a strong agreement between experiment and theory for values of  $\theta$  between  $25^\circ$  and  $30^\circ$  at all angles of  $\phi$  which corresponds to a tilted bilayer. Given the linear molecular structure, the lack of  $\phi$  dependence is not surprising, especially given the expected  $\phi$  variation of molecules at the nanorod ends. An additional apparent solution is shown at  $\theta = 90^\circ$  and  $\phi = 0^\circ$  and  $180^\circ$ . This solution could represent the DTAB laying down on the gold surface, but is most likely a spurious match between the experiment and theoretical values for  $R_{1-2}$  given the other evidence that similar surfactants form vertically oriented bilayers on gold nanorods.<sup>82</sup>

Mode	Ratio	Exp.	Calc. ( $\theta = 28^\circ, \phi = 0^\circ$ )
Trimethylammonium, 770 cm <sup>-1</sup>	r1	3.5	
CH2 Twist, 1450 cm <sup>-1</sup>	r2	1.4	
	R1-2	2.5	2.5

**Table 2: Ratio values at the optimal orientation for DTAB on gold nanorods.**

The tilted DTAB structure is consistent with other recent observations from cetyltrimethylammonium bromide (CTAB) on gold nanorods. CTAB is responsible for the synthesis of a variety of gold nanoparticles shapes, as well as cytotoxic effects.<sup>83</sup> Small angle X-ray scattering (SAXS), small angle neutron scattering (SANS), and transmission electron microscopy (TEM) indicate a surfactant layer that is 34 Å, which is intermediate between a CTAB monolayer (20 Å) and a CTAB bilayer (40 Å), leading to the conclusion that CTAB may form interdigitated bilayer structures.<sup>51, 82</sup> Although tilted bilayers were not initially considered, the  $\theta=28^\circ$  tilt observed here for DTAB accurately explains the TEM, SANS, and SAXS results for CTAB if it is similarly tilted.

#### 5.4. DOPC Membrane Structure

Beyond exploring surfactant layers as with DTAB, the structure of 9:1 DOPC:DOPG lipids was also explored with SABERS. The symmetric stretch of the lipid headgroup at 718 cm<sup>-1</sup> and the carbon chain double bond vibration observed at 1650 cm<sup>-1</sup> were used in the SABERS analysis. The full DOPC molecule is too large to for TDDFT calculation, so sections of the molecule were used, which is acceptable if the vibration modes studied are localized. The simulated headgroup and double

bond are shown in Figure 22 A. Similarity was calculated with the headgroup fixed at 5 Å above the gold surface, while the carbon double bond orientation and position were varied.

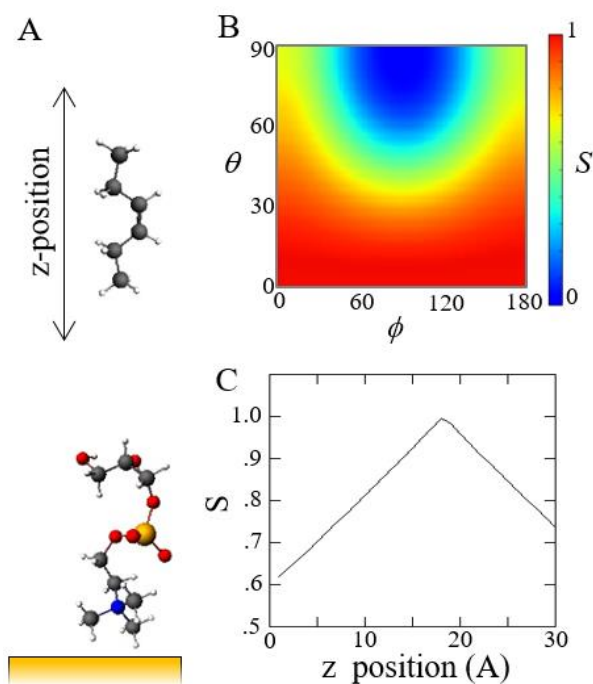


**Figure 22: SABERS analysis of the lipid membrane structure. A) The molecular structures analyzed in TDDFT were the phosphocholine headgroup positioned at 5Å above the gold particle surface, and the carbon double bond which was adjusted in z-position. B) The similarity map indicates a normally oriented fatty acid chain. C) The maximum similarity position at 18 Å, which is 13 Å past the headgroup.**

The results indicate the best matching similarity to be a  $\phi$ -independent band with the double bond oriented normal to the bilayer at  $\theta = 0^\circ$  as expected for a vertical bilayer structure. As the z-position is varied for the double bond, the maximum similarity is found at 18 Å from the gold surface. At 13 Å from the nitrogen atom in the phosphocholine headgroup, the SABERS result is in good

agreement with NMR data and molecular dynamics. The headgroup to double bond distance can be used as a measure of membrane thickness.

## 5.5. Tryptophan Orientation and Position

To further test SABERS on a membrane structure, the position and orientation of the amino acid tryptophan was studied in 9:1 DOPC:DOPG lipid bilayers. Tryptophan serves as an anchor for membrane proteins.<sup>84</sup> In Chapter 3 we showed that DOPC effectively displaces the native CTAB surfactant on gold nanorods, and forms a fluid bilayer on the surface with a fluid to gel transition temperature similar to empty lipid vesicles.<sup>74</sup>

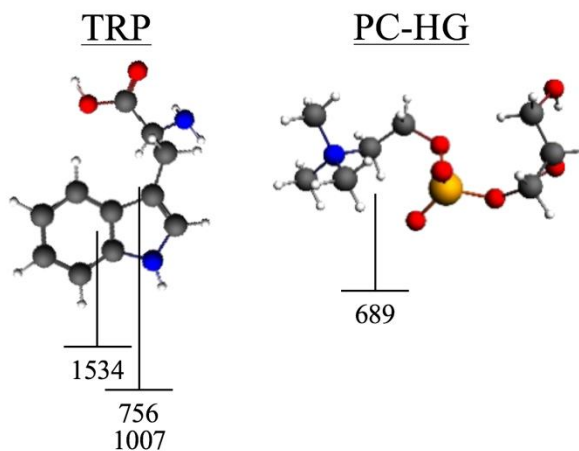


**Figure 23:** TDDFT optimized structure of tryptophan (TRP). Numerical labels indicate the positions and wavenumbers ( $\text{cm}^{-1}$ ) of the centers of vibration.

SERS and Raman spectra from DOPC bilayers with and without tryptophan are shown in Figure 24A. The peaks labeled with numerical identifiers are the

peaks used in the analysis. The symmetric stretch of the DOPC choline headgroup is labeled peak 1 and is identified in both the Raman (blue) and the SERS (red) spectra. The symmetric choline stretch is also clearly identified in the TDDFT calculation and shown in the figure (black). Only this Raman mode of DOPC was used for reference since we are most interested in the structure of tryptophan. The remaining peaks 2-4 are identified tryptophan peaks at 771, 1024, and 1562  $\text{cm}^{-1}$  and are clearly identified in the Raman, SERS, and TDDFT spectra. The centers of vibration for these modes are labeled in Figure 23. The tryptophan with DOPC SERS spectra was subtracted from the pure DOPC SERS to highlight the tryptophan modes by removing any overlapping peaks.

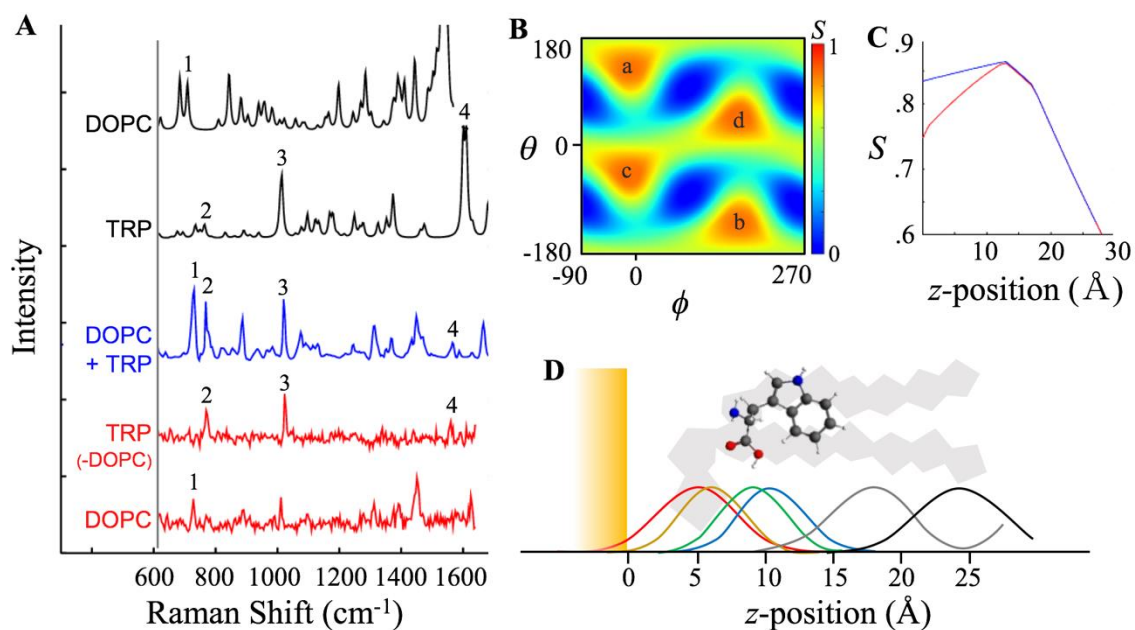


**Figure 24:** The orientation and position of tryptophan in DOPC bilayers according to SABERS. A) SERS spectra of DOPC and tryptophan in DOPC (red). Unenhanced Raman of lyophilized tryptophan in DOPC (blue). TDDFT calculated Raman of tryptophan and DOPC. Numbered peaks were used in the analysis. B) The similarity

map for all  $\theta$  and  $\phi$  at  $z = 13 \text{ \AA}$ . The peaks labeled a-d represent possible orientations.  
 C) Similarity as a function of z-position. The blue curve represents the maximum similarity of all orientations. The red curve is the similarity at orientation a in part B.  
 D) An illustration of the tryptophan position in the DOPC bilayer. The average positions of the lipid choline (red), phosphate (gold), glycerol (green), carbonyl (blue), alkane (gray), and  $\text{CH}_3$  (black) from SANS and SAXS measurements are included.<sup>85</sup> A coarse grain shaded figure of a relevant lipid structure is shown for reference.<sup>86</sup>

Using a vibrational mode of DOPC is not necessary in determining the orientation of tryptophan but is useful as a reference when determining relative position. For the similarity calculation, the DOPC headgroup z-position was fixed with the center of vibration for the  $728 \text{ cm}^{-1}$  symmetric stretch at  $5 \text{ \AA}$  from the gold surface. The orientation of the headgroup is irrelevant since the headgroup mode is highly symmetric. The ratios  $R_{1-2}$ ,  $R_{1-3}$ , and  $R_{1-4}$  were calculated for tryptophan at all values of  $\theta$ ,  $\phi$ , and  $z$  and sample values at a  $\theta$ ,  $\phi$ , and  $z$  solution are given in Table 3.

Mode	Ratio	Exp.	Calc. ( $\theta = 134^\circ$ , $\phi = 0^\circ$ , $z = 13 \text{ \AA}$ )
Choline, $720 \text{ cm}^{-1}$	$r_1$	.41	
Tryptophan, $740 \text{ cm}^{-1}$	$r_2$	.20	
Tryptophan, $1000 \text{ cm}^{-1}$	$r_3$	.21	
Tryptophan, $1550 \text{ cm}^{-1}$	$r_4$	.26	
	$R_{1-2}$	2.0	1.6
	$R_{1-3}$	1.9	1.9
	$R_{1-4}$	1.5	2.7

**Table 3: The ratio values for tryptophan at the optimal position and orientation in DOPC membranes.**

The similarity plot shown in Figure 24B displays the product of the similarities of these ratios at all  $\theta$  and  $\phi$ , for the z-plane that contains the maximum

similarity value of  $S=0.86$ . The similarity peaks labeled a and b correspond to mirror symmetric orientations that position the amino and carboxyl groups toward the interfacial region as expected.<sup>11,87,88</sup> Peaks c and d point in the opposite direction and likely correspond to the mathematically equivalent scenario of tryptophan sitting in an outer leaflet. Due to the symmetry of the Raman tensors, these mirrored symmetric solutions are indistinguishable but provide clear options for interpretation based on knowledge from previous studies. The c and d solutions are seen as spurious for our experiment due to this mathematical symmetry.

In addition to orientation, the z-position of tryptophan relative to the DOPC headgroup was studied. Figure 24C plots the similarity as a function of z-position of the tryptophan molecule. The peak at 13 Å locates the average center of vibration of the three modes analyzed, a position essentially on top of the C-3a atom. The SABERS orientation and position of tryptophan in a DOPC bilayer are depicted in Figure 24D, along with data from a combined X-ray and neutron scattering analysis of the DOPC bilayer structure.<sup>85</sup> The orientation result showing the long axis of the indole ring system  $46^\circ$  from the bilayer normal, is in good agreement with molecular dynamics and with linear dichroism measurements on aligned bilayers.<sup>11,87</sup> The z-position reported here matches the NMR measurements on tryptophan analogues that finds they interact strongly with the interfacial glycerol.<sup>88</sup> The z-position is also in agreement with atomistic molecular dynamics, which finds the energy minimum at the same location.<sup>87</sup> Since SABERS can be applied to multiple chemical groups within a membrane, it can be broadly applied to questions of membrane structure and membrane-protein interactions at high resolution and in ambient conditions.





## References

1. Singer, S. J.; Nicolson, G. L., The Fluid Mosaic Model of the Structure of Cell Membranes. *Science* **1972**, *175* (4023), 720-+.
2. Richter, R. P.; Berat, R.; Brisson, A. R., Formation of solid-supported lipid bilayers: An integrated view. *Langmuir* **2006**, *22* (8), 3497-3505.
3. Lipowsky, R.; Seifert, U., Adhesion of Vesicles and Membranes. *Molecular Crystals and Liquid Crystals* **1991**, *202*, 17-25.
4. Seifert, U., Configurations of fluid membranes and vesicles. *Advances in Physics* **1997**, *46* (1), 13-137.
5. Axelrod, D.; Koppel, D. E.; Schlessinger, J.; Elson, E.; Webb, W. W., MOBILITY MEASUREMENT BY ANALYSIS OF FLUORESCENCE PHOTOBLEACHING RECOVERY KINETICS. *Biophysical Journal* **1976**, *16* (9), 1055-1069.
6. Nagle, J. F.; Tristram-Nagle, S., Structure of lipid bilayers. *Biochimica Et Biophysica Acta-Reviews on Biomembranes* **2000**, *1469* (3), 159-195.
7. Li, T.; Senesi, A. J.; Lee, B., Small Angle X-ray Scattering for Nanoparticle Research. *Chemical Reviews* **2016**, *116* (18), 11128-11180.
8. Mason, P. C.; Gaulin, B. D.; Epand, R. M.; Katsaras, J., Critical swelling in single phospholipid bilayers. *Physical Review E* **2000**, *61* (5), 5634-5639.
9. Mason, P. C.; Gaulin, B. D.; Epand, R. M.; Wignall, G. D.; Lin, J. S., Small angle neutron scattering and calorimetric studies of large unilamellar vesicles of the phospholipid dipalmitoylphosphatidylcholine. *Physical Review E* **1999**, *59* (3), 3361-3367.
10. Balgavy, P.; Dubnickova, M.; Kucerka, N.; Kiselev, M. A.; Yaradaikin, S. P.; Uhrikova, D., Bilayer thickness and lipid interface area in unilamellar extruded 1,2-diacylphosphatidylcholine liposomes: a small-angle neutron scattering study. *Biochimica Et Biophysica Acta-Biomembranes* **2001**, *1512* (1), 40-52.
11. Esbjorner, E. K.; Caesar, C. E. B.; Albinsson, B.; Lincoln, P.; Norden, B., Tryptophan orientation in model lipid membranes. *Biochemical and Biophysical Research Communications* **2007**, *361* (3), 645-650.
12. Raman, C. V.; Krishnan, K. S., A new type of secondary radiation. *Nature* **1928**, *121*, 501-502.
13. Willets, K. A.; Van Duyne, R. P., Localized surface plasmon resonance spectroscopy and sensing. In *Annual Review of Physical Chemistry*, Annual Reviews: Palo Alto, 2007; Vol. 58, pp 267-297.
14. Mayer, K. M.; Hafner, J. H., Localized Surface Plasmon Resonance Sensors. *Chemical Reviews* **2011**, *111* (6), 3828-3857.
15. Dahlin, A.; Zach, M.; Rindzevicius, T.; Kall, M.; Sutherland, D. S.; Hook, F., Localized surface plasmon resonance sensing of lipid-membrane-mediated biorecognition events. *Journal of the American Chemical Society* **2005**, *127* (14), 5043-5048.

16. Galush, W. J.; Shelby, S. A.; Mulvihill, M. J.; Tao, A.; Yang, P. D.; Groves, J. T., A Nanocube Plasmonic Sensor for Molecular Binding on Membrane Surfaces. *Nano Letters* **2009**, *9* (5), 2077-2082.
17. Lee, T. H.; Heng, C.; Swann, M. J.; Gehman, J. D.; Separovic, F.; Aguilar, M. I., Real-time quantitative analysis of lipid disordering by aurein 1.2 during membrane adsorption, destabilisation and lysis. *Biochimica Et Biophysica Acta-Biomembranes* **2010**, *1798* (10), 1977-1986.
18. Schuller, J. A.; Barnard, E. S.; Cai, W. S.; Jun, Y. C.; White, J. S.; Brongersma, M. L., Plasmonics for extreme light concentration and manipulation (vol 9, pg 193, 2010). *Nature Materials* **2010**, *9* (4).
19. Moskovits, M., Surface-Enhanced Spectroscopy. *Reviews of Modern Physics* **1985**, *57* (3), 783-826.
20. Schatz, G. C.; Young, M. A.; Van Duyne, R. P., Electromagnetic mechanism of SERS. *Surface-Enhanced Raman Scattering: Physics and Applications* **2006**, *103*, 19-45.
21. Wang, D. S.; Chew, H.; Kerker, M., ENHANCED RAMAN-SCATTERING AT THE SURFACE (SERS) OF A SPHERICAL-PARTICLE. *Applied Optics* **1980**, *19* (14), 2256-2257.
22. Moskovits, M., Surface-enhanced Raman spectroscopy: a brief retrospective. *Journal of Raman Spectroscopy* **2005**, *36* (6-7), 485-496.
23. Kneipp, K.; Wang, Y.; Kneipp, H.; Perelman, L. T.; Itzkan, I.; Dasari, R.; Feld, M. S., Single molecule detection using surface-enhanced Raman scattering (SERS). *Physical Review Letters* **1997**, *78* (9), 1667-1670.
24. Golightly, R. S.; Doering, W. E.; Natan, M. J., Surface-Enhanced Raman Spectroscopy and Homeland Security: A Perfect Match? *Acs Nano* **2009**, *3* (10), 2859-2869.
25. Cao, Y. W. C.; Jin, R. C.; Mirkin, C. A., Nanoparticles with Raman spectroscopic fingerprints for DNA and RNA detection. *Science* **2002**, *297* (5586), 1536-1540.
26. Nie, S. M.; Emery, S. R., Probing single molecules and single nanoparticles by surface-enhanced Raman scattering. *Science* **1997**, *275* (5303), 1102-1106.
27. Kleinman, S. L.; Ringe, E.; Valley, N.; Wustholz, K. L.; Phillips, E.; Scheidt, K. A.; Schatz, G. C.; Van Duyne, R. P., Single-Molecule Surface-Enhanced Raman Spectroscopy of Crystal Violet Isotopologues: Theory and Experiment. *Journal of the American Chemical Society* **2011**, *133* (11), 4115-4122.
28. Michaels, A. M.; Jiang, J.; Brus, L., Ag nanocrystal junctions as the site for surface-enhanced Raman scattering of single Rhodamine 6G molecules. *Journal of Physical Chemistry B* **2000**, *104* (50), 11965-11971.
29. Lee, S.; Anderson, L. J. E.; Payne, C. M.; Hafner, J. H., Structural Transition in the Surfactant Layer that Surrounds Gold Nanorods as Observed by Analytical Surface-Enhanced Raman Spectroscopy. *Langmuir* **2011**, *27* (24), 14748-14756.
30. Kreisig, S. M.; Tarazona, A.; Koglin, E.; Schwuger, M. J., In situ analysis of cationic surfactants on electrode surfaces by FT-SERS microprobe spectroscopy .1. Adsorption of cetylpyridinium bromide. *Langmuir* **1996**, *12* (22), 5279-5288.

31. Weingart, J.; Vabbilisetty, P.; Sun, X. L., Membrane mimetic surface functionalization of nanoparticles: Methods and applications. *Advances in Colloid and Interface Science* **2013**, *197*, 68-84.
32. Troutier, A. L.; Ladaviere, C., An overview of lipid membrane supported by colloidal particles. *Advances in Colloid and Interface Science* **2007**, *133* (1), 1-21.
33. Al-Jamal, W. T.; Kostarelos, K., Liposome-nanoparticle hybrids for multimodal diagnostic and therapeutic applications. *Nanomedicine* **2007**, *2* (1), 85-98.
34. Levin, C. S.; Kundu, J.; Janesko, B. G.; Scuseria, G. E.; Raphael, R. M.; Halas, N. J., Interactions of Ibuprofen with Hybrid Lipid Bilayers Probed by Complementary Surface-Enhanced Vibrational Spectroscopies. *Journal of Physical Chemistry B* **2008**, *112* (45), 14168-14175.
35. Castellana, E. T.; Gamez, R. C.; Russell, D. H., Label-Free Biosensing with Lipid-Functionalized Gold Nanorods. *Journal of the American Chemical Society* **2011**, *133* (12), 4182-4185.
36. Yang, J. A.; Murphy, C. J., Evidence for Patchy Lipid Layers on Gold Nanoparticle Surfaces. *Langmuir* **2012**, *28* (12), 5404-5416.
37. Mabrey, S.; Sturtevant, J. M., Investigation of Phase-Transitions of Lipids and Lipid Mixtures by High Sensitivity Differential Scanning Calorimetry. *Proceedings of the National Academy of Sciences of the United States of America* **1976**, *73* (11), 3862-3866.
38. Naumann, C.; Brumm, T.; Bayerl, T. M., Phase-Transition Behavior of Single Phosphatidylcholine Bilayers on a Solid Spherical Support Studied by Dsc, Nmr and Ft-Ir. *Biophysical Journal* **1992**, *63* (5), 1314-1319.
39. Takahashi, H.; Niidome, Y.; Niidome, T.; Kaneko, K.; Kawasaki, H.; Yamada, S., Modification of gold nanorods using phosphatidylcholine to reduce cytotoxicity. *Langmuir* **2006**, *22* (1), 2-5.
40. Nakashima, H.; Furukawa, K.; Kashimura, Y.; Torimitsu, K., Self-assembly of gold nanorods induced by intermolecular interactions of surface-anchored lipids. *Langmuir* **2008**, *24* (11), 5654-5658.
41. Sitaula, S.; Mackiewicz, M. R.; Reed, S. M., Gold nanoparticles become stable to cyanide etch when coated with hybrid lipid bilayers. *Chemical Communications* **2008**, (26), 3013-3015.
42. Kundu, J.; Levin, C. S.; Halas, N. J., Real-time monitoring of lipid transfer between vesicles and hybrid bilayer on Au nanoshells using surface enhanced Raman scattering (SERS). *Nanoscale* **2009**, *1* (1), 114-117.
43. Lee, S. E.; Sasaki, D. Y.; Perroud, T. D.; Yoo, D.; Patel, K. D.; Lee, L. P., Biologically Functional Cationic Phospholipid-Gold Nanoplasmonic Carriers of RNA. *Journal of the American Chemical Society* **2009**, *131* (39), 14066-14074.
44. Orendorff, C. J.; Alam, T. M.; Sasaki, D. Y.; Bunker, B. C.; Voigt, J. A., Phospholipid-Gold Nanorod Composites. *Acs Nano* **2009**, *3* (4), 971-983.
45. Tam, N. C. M.; Scott, B. M. T.; Voicu, D.; Wilson, B. C.; Zheng, G., Facile Synthesis of Raman Active Phospholipid Gold Nanoparticles. *Bioconjugate Chemistry* **2010**, *21* (12), 2178-2182.

46. Kah, J. C. Y.; Zubieta, A.; Saavedra, R. A.; Hamad-Schifferli, K., Stability of Gold Nanorods Passivated with Amphiphilic Ligands. *Langmuir* **2012**, *28* (24), 8834-8844.
47. Lozano, N.; Al-Jamal, W. T.; Taruttis, A.; Beziere, N.; Burton, N. C.; Van den Bossche, J.; Mazza, M.; Herzog, E.; Ntziachristos, V.; Kostarelos, K., Liposome-Gold Nanorod Hybrids for High-Resolution Visualization Deep in Tissues. *Journal of the American Chemical Society* **2012**, *134* (32), 13256-13258.
48. Messersmith, R. E.; Nusz, G. J.; Reed, S. M., Using the Localized Surface Plasmon Resonance of Gold Nanoparticles To Monitor Lipid Membrane Assembly and Protein Binding. *Journal of Physical Chemistry C* **2013**, *117* (50), 26725-26733.
49. Yoo, J. H.; Han, H. S.; Lee, C.; Yoo, K. P.; Kang, T., Surface-Enhanced Raman Scattering-Based Detection of Molecules in an Aqueous Solution via Lipid-Modified Gold Nanorods. *Journal of Nanoscience and Nanotechnology* **2013**, *13* (11), 7239-7244.
50. Nikoobakht, B.; El-Sayed, M. A., Evidence for bilayer assembly of cationic surfactants on the surface of gold nanorods. *Langmuir* **2001**, *17* (20), 6368-6374.
51. Sau, T. K.; Murphy, C. J., Self-assembly patterns formed upon solvent evaporation of aqueous cetyltrimethylammonium bromide-coated gold nanoparticles of various shapes. *Langmuir* **2005**, *21* (7), 2923-2929.
52. Mehtala, J. G.; Zemlyanov, D. Y.; Max, J. P.; Kadasala, N.; Zhao, S.; Wei, A., Citrate-Stabilized Gold Nanorods. *Langmuir* **2014**, *30* (46), 13727-13730.
53. Dendramis, A. L.; Schwinn, E. W.; Sperline, R. P., A SURFACE-ENHANCED RAMAN-SCATTERING STUDY OF CTAB ADSORPTION ON COPPER. *Surface Science* **1983**, *134* (3), 675-688.
54. Gaber, B. P.; Yager, P.; Peticolas, W. L., Interpretation of Biomembrane Structure by Raman Difference Spectroscopy - Nature of Endothermic Transitions in Phosphatidylcholines. *Biophysical Journal* **1978**, *21* (2), 161-176.
55. Koglin, E.; Tarazona, A.; Kreisig, S.; Schwuger, M. J., In-situ investigations of coadsorbed cationic surfactants on charged surfaces: A SERS microprobe study. *Colloids and Surfaces, A: Physicochemical and Engineering Aspects* **1997**, *123*, 523-542.
56. Moskovits, M.; Suh, J. S., Conformation of Mono-Carboxylic and Dicarboxylic-Acids Adsorbed on Silver Surfaces. *Journal of the American Chemical Society* **1985**, *107* (24), 6826-6829.
57. Murphy, C. J.; San, T. K.; Gole, A. M.; Orendorff, C. J.; Gao, J. X.; Gou, L.; Hunyadi, S. E.; Li, T., Anisotropic metal nanoparticles: Synthesis, assembly, and optical applications. *Journal of Physical Chemistry B* **2005**, *109* (29), 13857-13870.
58. Hubert, F.; Testard, F.; Spalla, O., Cetyltrimethylammonium bromide silver bromide complex as the capping agent of gold nanorods. *Langmuir* **2008**, *24* (17), 9219-9222.
59. Gaber, B. P.; Peticolas, W. L., QUANTITATIVE INTERPRETATION OF BIOMEMBRANE STRUCTURE BY RAMAN-SPECTROSCOPY. *Biochimica Et Biophysica Acta* **1977**, *465* (2), 260-274.

60. Cherney, D. P.; Conboy, J. C.; Harris, J. M., Optical-trapping Raman microscopy detection of single unilamellar lipid vesicles. *Analytical Chemistry* **2003**, *75* (23), 6621-6628.
61. Gaber, B. P.; Yager, P.; Peticolas, W. L., Deuterated Phospholipids as Nonperturbing Components for Raman Studies of Biomembranes. *Biophysical Journal* **1978**, *22* (2), 191-207.
62. Sanderson, J. M.; Ward, A. D., Analysis of liposomal membrane composition using Raman tweezers. *Chemical Communications* **2004**, (9), 1120-1121.
63. Spiker, R. C.; Levin, I. W., Effect of Bilayer Curvature on Vibrational Raman Spectroscopic Behavior of Phospholipid-Water Assemblies. *Biochimica Et Biophysica Acta* **1976**, *455* (2), 560-575.
64. Spiker, R. C.; Levin, I. W., Phase-Transitions of Phospholipid Single-Wall Vesicles and Multilayers - Measurement by Vibrational Raman Spectroscopic Frequency Differences. *Biochimica Et Biophysica Acta* **1976**, *433* (3), 457-468.
65. Bayerl, T. M.; Schmidt, C. F.; Sackmann, E., Kinetics of Symmetric and Asymmetric Phospholipid Transfer between Small Sonicated Vesicles Studied by High-Sensitivity Differential Scanning Calorimetry, Nmr, Electron-Microscopy, and Dynamic Light-Scattering. *Biochemistry* **1988**, *27* (16), 6078-6085.
66. Needham, D.; Evans, E., Structure and Mechanical-Properties of Giant Lipid (Dmpc) Vesicle Bilayers from 20-Degrees-C Below to 10-Degrees-C above the Liquid-Crystal Crystalline Phase-Transition at 24-Degrees-C. *Biochemistry* **1988**, *27* (21), 8261-8269.
67. Reinl, H. M.; Bayerl, T. M., Lipid Transfer between Small Unilamellar Vesicles and Single Bilayers on a Solid Support - Self-Assembly of Supported Bilayers with Asymmetric Lipid Distribution. *Biochemistry* **1994**, *33* (47), 14091-14099.
68. Mclean, L. R.; Phillips, M. C., Kinetics of Phosphatidylcholine and Lysophosphatidylcholine Exchange between Unilamellar Vesicles. *Biochemistry* **1984**, *23* (20), 4624-4630.
69. Wimley, W. C.; Thompson, T. E., Transbilayer and Interbilayer Phospholipid Exchange in Dimyristoylphosphatidylcholine Dimyristoylphosphatidylethanolamine Large Unilamellar Vesicles. *Biochemistry* **1991**, *30* (6), 1702-1709.
70. Atkin, R., Mechanism of cationic surfactant adsorption at the solid-aqueous interface. *Advances in Colloid and Interface Science* **2003**, *103* (3), 219-304.
71. Chen, W. H.; Xu, X. D.; Jia, H. Z.; Lei, Q.; Luo, G. F.; Cheng, S. X.; Zhuo, R. X.; Zhang, X. Z., Therapeutic nanomedicine based on dual-intelligent functionalized gold nanoparticles for cancer imaging and therapy in vivo. *Biomaterials* **2013**, *34* (34), 8798-8807.
72. Jin, Y. D., Engineering Plasmonic Gold Nanostructures and Metamaterials for Biosensing and Nanomedicine. *Advanced Materials* **2012**, *24* (38), 5153-5165.
73. Webb, J. A.; Bardhan, R., Emerging advances in nanomedicine with engineered gold nanostructures. *Nanoscale* **2014**, *6* (5), 2502-2530.

74. Matthews, J. R.; Payne, C. M.; Hafner, J. H., Analysis of Phospholipid Bilayers on Gold Nanorods by Plasmon Resonance Sensing and Surface-Enhanced Raman Scattering. *Langmuir* **2015**, *31* (36), 9893-9900.
75. Le Ru, E. C.; Blackie, E.; Meyer, M.; Etchegoin, P. G., Surface enhanced Raman scattering enhancement factors: a comprehensive study. *Journal of Physical Chemistry C* **2007**, *111* (37), 13794-13803.
76. Doering, W. E.; Nie, S. M., Single-molecule and single-nanoparticle SERS: Examining the roles of surface active sites and chemical enhancement. *Journal of Physical Chemistry B* **2002**, *106* (2), 311-317.
77. Aikens, C. M.; Schatz, G. C., TDDFT studies of absorption and SERS spectra of pyridine interacting with Au-20. *Journal of Physical Chemistry A* **2006**, *110* (49), 13317-13324.
78. Valley, N.; Greeneltch, N.; Van Duyne, R. P.; Schatz, G. C., A Look at the Origin and Magnitude of the Chemical Contribution to the Enhancement Mechanism of Surface-Enhanced Raman Spectroscopy (SERS): Theory and Experiment. *Journal of Physical Chemistry Letters* **2013**, *4* (16), 2599-2604.
79. Long, D. A., *Raman Spectroscopy*. McGraw-Hill, Inc.: Great Britain, 1977; p 276.
80. Johnson, P. B.; Christy, R. W., OPTICAL CONSTANTS OF NOBLE METALS. *Physical Review B* **1972**, *6* (12), 4370-4379.
81. Neugebauer, J.; Reiher, M.; Kind, C.; Hess, B. A., Quantum chemical calculation of vibrational spectra of large molecules - Raman and IR spectra for buckminsterfullerene. *Journal of Computational Chemistry* **2002**, *23* (9), 895-910.
82. Gomez-Grana, S.; Hubert, F.; Testard, F.; Guerrero-Martinez, A.; Grillo, I.; Liz-Marzan, L. M.; Spalla, O., Surfactant (Bi)Layers on Gold Nanorods. *Langmuir* **2012**, *28* (2), 1453-1459.
83. Lohse, S. E.; Murphy, C. J., The Quest for Shape Control: A History of Gold Nanorod Synthesis. *Chemistry of Materials* **2013**, *25* (8), 1250-1261.
84. de Planque, M. R. R.; Kruijtzter, J. A. W.; Liskamp, R. M. J.; Marsh, D.; Greathouse, D. V.; Koeppe, R. E.; de Kruijff, B.; Killian, J. A., Different membrane anchoring positions of tryptophan and lysine in synthetic transmembrane alpha-helical peptides. *Journal of Biological Chemistry* **1999**, *274* (30), 20839-20846.
85. Kucerka, N.; Nagle, J. F.; Sachs, J. N.; Feller, S. E.; Pencer, J.; Jackson, A.; Katsaras, J., Lipid bilayer structure determined by the simultaneous analysis of neutron and x-ray scattering data. *Biophysical Journal* **2008**, *95* (5), 2356-2367.
86. Wang, Z. J.; Deserno, M., Systematic implicit solvent coarse-graining of bilayer membranes: lipid and phase transferability of the force field. *New Journal of Physics* **2010**, *12*.
87. MacCallum, J. L.; Bennett, W. F. D.; Tieleman, D. P., Distribution of amino acids in a lipid bilayer from computer simulations. *Biophysical Journal* **2008**, *94* (9), 3393-3404.
88. Yau, W. M.; Wimley, W. C.; Gawrisch, K.; White, S. H., The preference of tryptophan for membrane interfaces. *Biochemistry* **1998**, *37* (42), 14713-14718.

## Appendix A: Source Code

This appendix contains the documentation for the python code used in the SABERS calculation of position and orientation, which is done through calculation of similarity between experimental and theoretical SERS spectra. The code is written in Python and takes advantage of multiple packages all of which come standard with Python. These packages are: time, os, math, numpy, matplotlib, and scipy.ndimage.filters.

Since the source code itself is more than 1500 lines, copying it here would be excessive and less than helpful. Instead I will rather outline the various files and packages involved, and include comments for a general explanation about how each piece works. More detailed descriptions can be found in the comments throughout the source code. The following sections are arranged by filename and then by function as it appears within the corresponding file.

### **calculate\_spectrum.py**

This module defines the functions for calculating the Raman spectra including the actual peak intensities given the Polarizability Tensor (aka `alpha_tensor`), electric field as a function of `z` (distance from the gold surface), and the center of vibration for a given frequency. The following are the functions in this file:

**calculate\_full\_raman(new\_alpha, peaks\_to\_compare)**

This function returns a variable named 'full\_alpha' which is the Raman intensities for a randomly oriented molecule. This function calculates the full Raman contributions given by the expression:

$$I(\pi/2) \propto (45a'^2 + 7\gamma'^2)/45$$

where  $a'$  and  $\gamma'$  are given by:

$$a = 1/3(\alpha_{xx} + \alpha_{yy} + \alpha_{zz})$$

$$\gamma^2 = \frac{1}{2} \left( (\alpha_{xx} - \alpha_{yy})^2 + (\alpha_{yy} - \alpha_{zz})^2 + (\alpha_{zz} - \alpha_{xx})^2 + 6(\alpha_{xy}^2 + \alpha_{yz}^2 + \alpha_{zx}^2) \right)$$

The output 'full\_alpha' contains the Raman peak heights for a randomly oriented molecule, but for efficiency only the Raman intensities for the frequencies indicated by 'peaks\_to\_compare' are calculated. The full Raman contribution is calculated as:

$$full\_alpha = (45a(\omega)^2 + 7\gamma(\omega)^2)/45$$

where both  $a$  and  $\gamma$  are functions of the frequency  $\omega$  in units of wavenumbers ( $cm^{-1}$ ).



**sparse\_intensity(rotation\_vector, peaks\_to\_compare, center\_of\_vibration,  
alpha\_tensor, a\_tensor, z\_position, frequencies)**

This function returns the variable 'intensity\_alpha' which is the SERS intensity for SERS peaks at the frequencies specified by 'peaks\_to\_compare'. This is the function used in the main loop of the code. This function takes in 7 variables and does two things: First, it rotates the center\_of\_vibration, the alpha\_tensor, and the A\_tensor to match the orientation of the molecule. The other thing this function does is it calls the calculate\_full\_raman and calculate\_intensities functions for calculating the SERS peak intensities for the specific molecular position/ orientation.

Since this function is called in a large loop, we limit the number of frequencies we use for the calculation to only those peaks used for the comparison. This cuts the number of calculations at each iteration down to only two or three frequencies. This speeds up the calculation by orders of magnitude. You'll notice that we use peaks\_to\_compare for a lot of the loops here for that reason. Look for expressions like 'for peaks in peaks\_to\_compare' indicating we only do the calculation for certain frequencies. Also recall that peaks\_to\_compare contains the indices for the frequencies we are interested in.

**calculate\_intensities(dia, peaks\_to\_compare, wavenumber, full\_alpha,  
new\_alpha\_zz, new\_a\_zzz, z\_cent)**

This function returns the variable 'intensity' which is the calculated SERS intensity. This is the function where we calculate the SERS intensity at each frequency. The variable 'full\_alpha' is used here to divide the  $\alpha$  component.

A note on the *numpy* package: Since we are using *numpy* arrays (just a special python package for arrays) we can do simple math operations on a vector or array, and python understands to do that operation on each element in the array. For example *math.exp()* only works on a single number but *numpy.exp()* can operate on a each element in a vector or matrix. It's pretty nice and saves us having to use lots of for loops which are slow. Child functions that are called here such as 'efields' also utilize the *numpy* package.

### **efields.py**

This simple function defines the efield and efield Gradient near the gold nano particle surface as a function of both distance from the gold surface (*z\_position*) and wavenumber.

#### **e\_field(diameter, z\_position, wavenumber)**

The efield function for either 25nm or 50nm diameter Au NRs.

#### **grad\_efield(diameter, z\_position, wavenumber)**

The Gradient efield function for either 25nm or 50nm diameter Au NRs.

## **euler\_rotate.py**

This module contains the functions for finding a rotation matrix, and using that matrix to rotate a vector and a 3x3 matrix such as a tensor.

### **find\_rotation\_matrix(rotation\_vector)**

This is a function that uses a rotation vector  $(\psi, \theta, \phi)$  to get the resulting rotation matrix. Use of the numpy library for the trigonometric calculations of cos and sin allow for the functions to operate on an entire array in one step, providing the ability for parallelization of rotation matrix calculations. The function outputs a 3x3 rotation matrix called *rotation\_matrix* (creatively).

### **vector\_rotate(vector, rotation\_matrix)**

This function rotates a given  $(x, y, z)$  vector by a rotation matrix. Essentially, this function simply performs a dot product. The function outputs the rotated vector as the variable *vector\_prime*.

### **order\_2\_tensor\_rotate(tensor, rotation\_matrix)**

Using a rotation matrix  $Q$ , this function rotates a given order 2 tensor  $T$ , namely a 3x3 matrix using the following formula:

$$T'_{ij} = Q_{ip}Q_{jq}T_{pq}$$

**order\_3\_tensor\_rotate(tensor, rotation\_matrix):**

Using a rotation matrix  $Q$ , this function rotates a given order 3 tensor  $T$ , namely a 3x3x3 tensor. This is done using the tensor rotation formula:

$$T'_{ijk} = Q_{ip}Q_{jq}Q_{kr}T_{pqr}$$

**order\_3\_tensor\_rotate\_zzz(tensor, rotation\_matrix):**

Using a rotation matrix  $Q$ , this function rotates a given order 3 tensor  $T$  using the same formula as in **order\_3\_tensor\_rotate**, but this function only calculates the rotation for the  $(z, z, z)$  element i.e.  $T_{333}$ . By reducing the transformation to only one element, the calculation is much more efficient for checking every orientation of a molecule.

**rotate\_molecule(rotation\_vector, atom\_data)**

This function takes the atom coordinate data for a molecule, and rotates each atom  $(x, y, z)$  position by the rotation vector  $(\psi, \theta, \phi)$ . This function utilizes the rotation matrix  $Q$  and the functions **find\_rotation\_matrix** and **vector\_rotate**. Since I was using these functions together a lot of the time, I decided it made sense just to make this its own function.

**orient\_tryptophan(atom\_data)**

Tryptophan was run in ADF at a strange orientation. In order to assure that TRP is well oriented for our calculation, we center and orient the TRP molecule. As

long as the atom numbering remains unchanged, this function will work generally for a TRP molecule in any orientation or position. The straightening protocol is somewhat sensitive to round off error since it uses radians. There's probably a better way to do this, but it works ok for now so I'll leave it. Check source code comments for more details on the alignment of tryptophan.

### **orient\_naphthol(atom\_data)**

Returns the rotated naphthol molecule *atom\_data*, and the *rotation\_vector* ( $\psi, \theta, \phi$ ) used to rotate the molecule. This function aligns naphthol and centers the molecule. Since the molecule is already well aligned (rotated), this function really only serves to center (translate) the naphthol molecule. You can therefore see that the rotation vector is fixed to  $(0, 0, 0)$ .

### **main\_loop\_single\_mol.py**

This is the main module for analyzing ADF data and comparing with experiment to determine the most likely molecule orientation based on ratios of peak heights. This version of the main loop only looks at a single molecule for the spectra comparisons. This is the module used to run the CTAB analysis. Following the script here and reading the comments should reveal how the code is working.

### **main\_loop\_two\_mol.py**

This is the main loop for calculating molecular orientation using a separate molecule as a reference. It works very similar to **main\_loop\_single\_mol.py** except that here we use the *FIXED\_MOL* as the reference spectral peak. The file **main\_loop\_single\_mol.py** might be commented better so if there is something you don't understand, it would probably help to look at that file first to get an idea for things, since this function is based on that one. This is the module used for the tryptophan and DOPC double bond orientations.

### **main\_loop\_z\_dependence.py**

This module is for running the z-dependence analysis for finding how far a molecule is from the gold surface. Recall that the z-dependence can only be accurately determined by having a fixed reference molecule i.e. *FIXED\_MOL*, so by default, this module works for the Tryptophan/ DOPC experiment, but not for plain CTAB. It works similar to **main\_loop\_two\_molecules.py**, except that here we fix the theta and phi orientation and plot the similarity as a function of z position only.

### **maxima\_finder.py**

These are functions I wrote for finding local maxima on data. It's mostly useful for spitting out every local maximum in a color map plot or spectra. It's helpful for speeding up the processing of data.

**local\_maxima\_1d(data)**

Finds local maxima on an array of data. 'data' would be like your y-values for a spectrum. The function returns y-value maxima indices, and could also return the actual y-values.

**local\_maxima\_projection(data\_1, data\_2, data\_3, threshold)**

I'm not currently using this function. This function finds local maxima on 2D data  $f(x, y)$  by treating  $x$  and  $y$  as independent variables. This function finds the local maxima for  $f(x)$  and then find the local maxima for  $f(y)$ . A threshold is defined based on  $f(x, y)$ .

**local\_maxima\_3d(x\_data, y\_data, z\_data, threshold)**

This is the function I used to find local maxima. It avoids sharp features (think of hot pixels of very small diameter in an image) and features too close to the edge (since a rising slope at the edge of the photo is a local maxima, but may not be the maxima of the feature). Uses 3D  $x$ ,  $y$ , and  $z$  data ( $z$  is an  $x$  by  $y$  array, and  $x$  and  $y$  are vectors). Finds local maxima based on `neighbor_size`, `threshold`, and `edge_boundary`. Returns the  $x$ ,  $y$  indices for each local maxima as a 2 by  $N$  array, where  $N$  is the number of local maxima.

## **parse\_data.py**

This module contains all the functions needed for parsing the necessary information from the ADF output file for calculating the Raman peak intensities based on the Polarizability Tensor, centers of vibration, atom positions, bonds, and Polarizability Gradient. For most variables (except for `atom_data` and `bond_data`) the variables are saved as a list with at least one dimension corresponding to frequency. For example: The `centers_of_vibration` variable is saved as a `[N,3]` list where `N` is the number of Raman frequencies for the particular molecule, and `3` is for the `x`, `y`, and `z` coordinates of the vibration's center.

### **find\_atoms(filename)**

This function finds the atoms `x`, `y`, `z` coordinates from the ADF output file. `atom_data` is an `[A, 3]` array where `A` is the number of atoms.

### **find\_bonds(filename, atom\_data)**

Finds the bonds between atoms and is only used for plotting purposes. `bond_data_x`, `bond_data_y`, and `bond_data_z` are `[B, 2]` arrays where `B` is the number of atomic bonds in the molecule. Looking at the first column in each array would be representative of the first bond's starting and ending coordinates, ie the first bond starts at `bond_data_x[0,0]`, `bond_data_y[0,0]`, `bond_data_z[0,0]`, and terminates at `bond_data_x[0,1]`, `bond_data_y[0,1]`, `bond_data_z[0,1]`.



**find\_frequencies(filename)**

Finds the frequencies of vibrations from the output file. frequencies is a 1-D array of length N.

**find\_alpha\_tensor(filename):**

Finds the Polarizability Tensor alpha. alpha\_tensor is a [N, 3, 3] array.

**find\_a\_tensor(filename):**

Finds the Gradient Polarizability Tensor denoted 'A'. a\_tensor is a [N, 3, 3, 3] array.

**find\_displacement\_indicies(filename):**

Finds the indicies for the displacement function. I found that it was easier to break up the displacement and displacement indicies into two funtions.

**find\_displacements(filename):**

Finds the magnitudes of displacement for each vibrational mode. 'displacements' is a [N, A, 3] array where N is the number of frequencies, A is the number of atoms, and 3 is for the x, y, z coordinates of the displacement magnitude.

**find\_centers(filename, atom\_data):**

Finds centers of vibration for each vibrational frequency. center\_of\_vibration is an [N, 3] array where N is the number of frequencies.

## **plot\_data.py**

This module contains various functions for plotting data. If you couldn't figure that out, I can't help you ;-).

### **plot\_molecule(atom\_data, center\_of\_vibration, filename)**

This function plots the molecule in 3D with lines representing atom bonds and circles representing the atoms. Also includes points representing the centers of vibration for the various modes.

### **plot\_molecule\_movie(atom\_data, center\_of\_vibration, filename, vec)**

This function plots the molecule in 3D with lines representing atom bonds and circles representing the atoms. Also includes points representing the centers of vibration for the various modes. This function goes one step further by plotting the molecule at iterated rotations about the z axis and stitches these plots together in a gif video.

### **plot\_simple\_spectrum(x\_data, y\_data)**

This is a simple x, y line plot. Useful for plotting simple spectra.

### **plot\_spectrum(x\_data, y\_data, labels)**

This is a simple x, y line plot. This version also takes the variable 'labels' which is a list including the 'x-label' and 'y-label' for the x and y axes, and also the variable 'fname' for saving the png of the plot and also a csv with the plot data.

**map\_plot(x\_value, y\_value, z\_value, labels)**

Plots a x, y, z color map with z represented as the color. This is mostly used for the color contour plots for the theta, phi, similarity plots. The function takes in x-value, y-value, z-value, and labels. 'Labels' is a list including the x-label, y-label, and fname for saving the png of the plot.

**map\_plot\_maxima(x\_value, y\_value, z\_value, maxima, labels)**

Plots a x, y, z color map with z represented as the color. This version of map plot also includes highlighting the maxima with black circles. This is useful for visually marking the local maxima on the color plots, which can sometimes be hard to identify with the eye.

**molecule\_data.py**

This module contains the experimental data for the SERS and RAMAN spectra, as well as the peak heights for the ADF RAMAN, for all molecules we're interested in.

**load\_mol\_data(sample)**

Loads the relevant data for a given molecule. The variable *sample* is parsed from the filename used to load the ADF data.

**process\_molecule.py**

This is a simple program to take a filename, rotation vector and translation vector and plot the oriented molecule.

**orient\_molecule(filename)**

Takes the filename and outputs a centered and aligned molecule ready for rotation and calculations.

**plot\_rotated\_molecule(filename, rotation\_vector, z\_position, gif)**

This function takes the molecule filename, a rotation matrix and z position, and a boolean variable called 'gif' which either makes a gif or simply plots a single image of the molecule at the position and orientation specified. Mainly this is used for visualizing the molecular orientations from the analysis.